Wound-Induced Syncytia Outpace Mononucleate Neighbors during *Drosophila* Wound Repair

James S. White[1,2], Junmin Hua[1,2] , Jasmine J. Su[1,4], Kaden J. Tro[3], Elizabeth M. Ruark[1,2], M. Shane Hutson[3,4*], Andrea Page-McCaw[1,2,5,6*]

***Correspondence:**

andrea.page-mccaw@vanderbilt.edu

shane.hutson@vanderbilt.edu

Author contributions: Conceptualization, J.S.W., J.H., A.P.M., M.S.H.; Formal Analysis, J.S.W., J.H., J.J.S., K.T.; Investigation, J.S.W., J.H., J.J.S., E.M.R., J.H.; Writing – Original Draft., J.S.W., A.P.M.; Visualization, J.S.W., J.J.S.; Supervision, A.P.M., M.S.H., J.S.W. ; Project Administration, J.S.W., A.P.M., M.S.H; Funding Acquisition, A.P.M., M.S.H

[1]Dept. Cell and Developmental Biology, Vanderbilt School of Medicine, Nashville, TN

[2]Program in Developmental Biology, Vanderbilt University Nashville, TN

[3]Dept. Physics and Astronomy Vanderbilt University Nashville, TN

[4]Dept. Biological Sciences, Vanderbilt University, Nashville, TN

[5]Vanderbilt-Ingram Cancer Center, Vanderbilt University, Nashville, TN

[6]Lead Contact

*Corresponding Authors

ABSTRACT:

In response to injury, cells proliferate, migrate and invade to replace missing cells and close wounds. However, the role of other wound-induced cell behaviors is not understood, including the formation of syncytia (multinucleated cells). Here, we use *in vivo* live imaging to analyze wound-induced syncytia in mitotically competent *Drosophila* pupae. We find that almost half the epithelial cells near a wound fuse to form large syncytia. When the autophagy gene *Atg1* is knocked down, fewer syncytia form, and wounds close more slowly. Further, a computational model of tissue fluidity indicates that cell fusion speeds wound closure time by about one third. Syncytia use several routes to speed wound repair: they outpace diploid cells at the wound margin to lead the initial resealing of the wound; they reduce the need for intercalation as the tissue reshapes during closure; and they pool resources of their component cells to concentrate them toward the wound margin. In addition to wound healing, these properties of syncytia are likely to contribute to their roles in development and pathology.

INTRODUCTION

Injury is a constant reality of life, and survival requires all organisms to repair wounds. Wound-induced cell behaviors like proliferation, migration, and invasion replace missing cells and close wounds (Martin et al., 2024). Other cell behaviors are induced around wounds, but their contribution to wound healing is not well understood, *e.g.*, the fusion of cells into syncytia. Syncytia are one type of polyploid cell, and it is generally appreciated that increases in ploidy – number of genomes per cell – is a common response of post-mitotic tissues and cells to injury (Losick et al., 2013; Nandakumar et al., 2020; Tamori and Deng, 2013). Wound-induced epithelial syncytia were first observed around epidermal puncture wounds in *Drosophila* larvae and adults (Galko and Krasnow, 2004; Losick et al., 2013), consistent with the idea of polyploidy induction in non-proliferative cells. However, recent studies have observed syncytia around wounds in mitotically competent tissues: around laser-ablation wounds in *Drosophila* pupal epidermis (Wang et al., 2015) and in zebrafish epicardium damaged by endotoxin, microdissection, or laser ablation (Cao et al., 2017). Further, injury associated with the surgical implantation of biomaterials can cause immune cells to fuse into multinucleated giant cells, which are associated with rejection (Al-Maawi et al., 2017). Similarly, injury induces bone marrow-derived cells to fuse with various somatic cells to promote repair (Alvarez-Dolado et al., 2003; Corbel et al., 2003; Davies et al., 2009; Nygren et al., 2004). The many instances of syncytia being induced by wounds raise the possibility that syncytia offer an adaptive benefit. It is not clear, however, what that benefit is.

Syncytia can form either by endomitosis – mitosis without cytokinesis – or by cell-cell fusion. Fusion is widely observed throughout development in both vertebrates and invertebrates: for example myoblasts fuse into muscles (Kim et al., 2015a; Lehka and Rędowicz, 2020), and

60 fusions occur in the lineages of the *C. elegans* hypodermis (Podbilewicz and White, 1994) as
61 well as vertebrate trophoblast (Renaud and Jeyarajah, 2022) and osteoclast (Søe, 2020). Cell
62 fusions are also observed in disease: pathogen-induced epithelial fusion allows spreading of
63 many viruses including human respiratory syncytial virus and SARS-CoV-2 (Leroy et al., 2020);
64 and the fusion of cancer cells with bone-marrow derived cells is implicated in metastasis
65 (Pawelek and Chakraborty, 2008).

66 Here, we use live imaging and clonal analysis to understand the behavior of syncytia
67 following laser wounding in the *Drosophila* pupal notum. The unwounded notum is a monolayer
68 epithelium composed of mononuclear diploid cells that are mitotically competent. Nonetheless,
69 during the first several hours after wounding, many of the surrounding cells fuse to form giant
70 syncytia. We previously reported that after wounding the pupal notum, some wound-adjacent
71 cells undergo a single round of endoreplication, increasing their ploidy two-fold (White et al.,
72 2024), but fusion increases ploidy far more, with some wound-induced syncytia observed to have
73 more than a dozen nuclei. Some cell fusions are obvious with apical borders breaking down
74 between cells, while others surprisingly appear as shrinking of a cell's apical surface. Combined,
75 fusion is a common fate of cells near wounds: about half the cells fuse to form syncytia within 70
76 µm of a wound with 30 µm radius. To understand the role of fusion-mediated syncytia in wound
77 repair, we undertook two types of analysis, first analyzing an autophagy mutant that reduces
78 fusion after wounding, and second comparing the behaviors of syncytial and mononuclear cells
79 within the same wound. Compared to their smaller mononuclear neighbors, syncytia outpace
80 mononuclear cells to the leading edge. We propose that syncytia accelerate wound repair because
81 cell fusion limits the need to negotiate cell intercalations as the wound closes, a hypothesis

82 supported by computational modeling; and because clonal analysis demonstrates that syncytia

83 mobilize and transport cell resources such as actin from distal cells to the wound margin.

84

85 **RESULTS:**

86 **A mitotic tissue utilizes cell-cell fusions during wound repair.**

87 The pupal notum is a monolayer columnar epithelium that will become the epidermis of
88 the adult fly. At the time of our analysis, 12-18h after puparium formation (APF), it sits atop a
89 basement membrane that is still developing (Mehaffey et al., 2024), and it is composed of diploid
90 cells that undergo regular mitotic cycles (Guirao et al., 2015) (Figure 1—figure supplement 1A-
91 C). To analyze cell behaviors around wounds, we live-imaged after laser ablation. Epithelial cell
92 borders were labeled by the adherens junction protein p120ctnRFP (Ogura et al., 2018) and
93 nuclei were labeled with histone His2GFP. Two hours after wounding, we observed what
94 appeared to be prominent syncytial (multi-nucleated) cells around the wound (Figure 1A);
95 experiments described below demonstrated that these were indeed syncytia. Some appeared to
96 contain over a dozen nuclei within epithelial borders. For both syncytial and mononuclear cells,
97 it was difficult to assign nuclei precisely to cell borders because notum epithelial cells are not
98 oriented at right angles with respect to the surface, and in 2-D projections, a nucleus was
99 frequently observed outside the cell's apical border (Figure 1—figure supplement 1D).
100 Accordingly, using apical area and nuclear density, we estimated the number of nuclei within the
101 3 largest syncytia in different wounds. The number of nuclei in these syncytia increased over
102 time: at 1 h after wounding the three largest syncytia contained an average 3-13 nuclei, and 2 h
103 after wounding they nearly doubled to 6-20 nuclei (Figure 1B). Interestingly, larger wounds
104 generated syncytia with larger apical areas and more nuclei, proportional to wound size,
105 suggesting syncytium formation is a dynamic and scalable response to injury (Figure 1 C-E).

106 Live imaging of cells after wounding revealed the gradual loss of p120ctn along the
107 border between two epithelial cells followed by rounding of the resulting syncytium (Figure 1F,I,

108 and Video 2), such that the initial two-cell morphology gradually became a one-cell morphology.
109 We termed the visible loss of p120ctn "border breakdown". We determined that as p120ctn was
110 lost, the adherens junction protein E-cadherin was also lost (Figure 1—figure supplement 1E-H)
111 indicating adherens junctions disassembly along the border between the cells. Border
112 breakdowns were found spatially clustered in the first three to four rows of cells, 30-50 μm from
113 the wound center, and they occurred primarily within the first hour after wounding, some within
114 10 minutes after wounding (Figure 1G,H). These events could be explained by wound-induced
115 cell fusion or by wound-induced epithelial-to-mesenchymal transition. To ask whether border
116 breakdowns represented cell fusions, we analyzed cytoplasmic mixing. Individual GFP-labeled
117 cells (clones) were generated at random locations using the flip-out Gal4 technique (Pignoni and
118 Zipursky, 1997). Before wounding, the level of cytoplasmic GFP fluorescence was stable yet
119 exhibited cell-to-cell variability, allowing some differentiation of cells by intensity (Figure 1I^{i}).
120 Minutes after a nearby laser ablation, GFP was observed to diffuse from labeled cells into
121 neighboring unlabeled cells. GFP mixing between two cells was followed by the eventual loss of
122 their shared p120ctn-labeled cell border, confirming that border breakdown is indeed cell fusion,
123 but that cytoplasmic mixing occurs more than 10 minutes before the border breakdown is first
124 observed to start (Figure 1I, Video 2). GFP mixing always preceded border breakdowns (n=11).
125 Cytoplasmic GFP mixing resulted in a consistent level of fluorescence across the two cells,
126 indicating that GFP mixing is a reliable indicator of plasma membrane fusion. The order of
127 events demonstrates that plasma membrane fusion occurs many minutes before the visible
128 disassembly of the apically located adherens junctions. Thus, epithelial fusion is a rapid local
129 response to wounding, and border breakdown is a lagging indicator of cell fusion.
130

131 **Apical cell shrinking also represents cell-cell fusion, evident later during wound closure.**

132 Border breakdowns, representing cell fusion events, occurred mostly within 1 h after
133 wounding, so it was unclear how syncytia grew in size and nuclear number between 1-2 h after
134 wounding. However, an unexpected cell behavior was frequently observed during this time: the
135 apical area of diploid epithelial cells shrank until they disappeared from the epithelial sheet, a
136 phenomenon we termed "apical shrinking" (Figure 2A). Although the appearance of apical
137 shrinking suggested cell extrusion, we were surprised at its high frequency around wounds
138 (Figure 2E), as wounds have already lost many cells and would be expected to prioritize cell
139 survival to speed barrier repair. To understand the fate of apical-shrinking cells, we tracked their
140 nuclei and determined that they did not extrude; rather, all apical-shrinking cell nuclei moved
141 laterally within the plane of the epithelium to join neighboring syncytia (n=7, Figure 2B),
142 suggesting that apical shrinking is an indicator of cell fusion. To better understand this behavior,
143 we analyzed individual GFP-labeled cells so that we could observe the fate of the cytoplasm.
144 Like with border breakdowns, GFP mixing in the X-Y plane of the epithelium was observed to
145 precede the initiation of apical shrinking, although the interval between GFP mixing and apical
146 shrinking was longer, one or more hours (Figure 2C, Video 3). In X-Z projections, GFP labeled
147 cytoplasm associated with apical shrinking shifted laterally to join with a neighboring cell as
148 shown for two apical-shrinking cells in Figure 2D. For the cell labeled with the yellow arrow,
149 before apical shrinking at 60 min post wound, its GFP-labeled cytoplasm extended from the
150 plane of the adherens junctions (Z_{AJ}) basally over 8 μm; when apical shrinking was underway at
151 120 min post wound, its cytoplasm extended less than 5 μm down from the apical plane; and
152 when shrinking was almost complete at 150 min post wound, it extended only 1-2 μm down
153 from the apical plane, appearing as a whisp of cytoplasm connecting the shrinking apical surface

154 with the neighboring syncytia. A similar loss of basal depth over time is observed in the cell
155 labeled with the white arrow. In both these cells, as the cell lost its basal volume, cytoplasm
156 moved laterally to join the neighboring syncytia. Thus, analysis of both nuclei and cytoplasm
157 demonstrated that apical shrinking represented cell fusion events. The spatial distribution of
158 apical shrinking around wounds was similar to border breakdowns, but fusions associated with
159 apical shrinking occurred later and were more numerous (Figure 2E,F). Thus, cell fusion is
160 evident as either border breakdown or apical shrinking, which both occur after GFP sharing.
161 To determine what percentage of cells around a wound will fuse, we analyzed over 100
162 single epithelial cells randomly-labeled with cytoplasmic GFP within the radius of observed
163 fusion (80 µm), tracking them for 6.5 h to assess their fate (Figure 3A,B): a full quarter of the
164 cells fused (25%), sharing GFP before borders breakdown or apical shrinking; 67% persisted as
165 diploid cells, most with stable GFP, but infrequently (n=3) with GFP mixing and no subsequent
166 cell fusion; the remaining 7% could not be tracked (Figure 3—figure supplement 1A). All GFP-
167 labeled cells with apical shrinking had previously shared cytoplasm, indicating that all apical
168 shrinking represents fusion. The observation of rare diploid cells with previous cytoplasmic
169 mixing confirms that plasma membrane fusion occurs before the later steps of border
170 breakdown/apical shrinking, as these cells represent fusion initiation events (fusion pore) but
171 were unable to productively stabilize and expand the site of fusion and so returned to the diploid
172 state. Fusing cells were strongly skewed toward the center of the wound: within 70 µm, about
173 half the cells (47%) underwent fusion (Figure 3A, left), and fusion continued for over 300 min
174 after wounding (Figure 3—figure supplement 1B,C). Apical shrinking accounts for more than
175 half of all fusing cells (Figure 3C), and the spatial distribution of fusing cells that shrank vs. lost
176 borders was similar (compare Figures 1G and 2E). However, apical shrinking began later than

177 border breakdowns (Figure 2F, Figure 3—figure supplement 1C), continued for several hours
178 after wounding (Figure 2F, Figure 3—figure supplement 1C), and took longer to complete
179 (Figure 3—figure supplement 1D). Thus, fusion associated with apical shrinking accounted for
180 continuing syncytial growth after border breakdowns subsided. Further, cell fusion is a persistent
181 behavior over the course of wound closure.

182 Our individual cell tracking indicated that syncytia were the result of epithelial cell
183 fusions. However, phagocytic hemocytes are known to migrate to the sites of pupal wounds
184 (Antunes et al., 2013). To determine if hemocytes fused with epithelial syncytia around wounds,
185 we labeled hemocytes with cytoplasmic GFP (*hml>GFP*) and observed their behavior in live
186 imaging. In six wounds, we observed GFP-labeled hemocytes at the basal side of the wound
187 margin; however, we did not observe any events where GFP was transferred from hemocytes to
188 the epithelium, ruling out the fusion of hemocytes with epithelia in pupal wounds (Supplemental
189 Video 4) .

190

191 **Syncytia close wounds faster.**

192 To evaluate the role of cell fusion and syncytia in repairing wounds, we wanted to
193 analyze a mutant that blocked syncytia formation. It has been reported that several individual
194 autophagy (*Atg*) genes are required for syncytia formation around small laser ablation wounds in
195 the polyploid *Drosophila* larval epithelium (Kakanj et al., 2022), so we asked if autophagy
196 promotes fusion around laser wounds in the diploid pupal epithelium. Using a dsRNA line
197 known to disrupt syncytia in larvae, we knocked down *Atg1* on one side of the wound expressing
198 *pnr-Gal4*, as illustrated in Figure 4A, reserving the other side of the wound as an internal control,
199 modifying an internally controlled wounding system we have previously reported (O'Connor et

200 al., 2021b). Visualizing Ecad-labeled cell borders across the wound, we found that indeed *Atg1* is
201 required for syncytia formation in pupal wounds, like it is in larval wounds (Figure 4B).
202 Specifically, we observed a reduction in cell fusion, both reductions of border loss and apical
203 shrinking (Figure 4C). We next compared wound closure rates on the two sides of the wound
204 (Figure 4D,E). Because leading edge migration is slightly delayed on the *pnr-Gal4* side of the
205 wound even in control wounds (*pnr*>+), we compared the difference in wound radii on the two
206 sides, comparing control wounds to *pnr>Atg1*^{RNAi} wounds. By 5h after wounding, the *pnr*>+ side
207 lagged behind the other side by only about 10 µm, yet the *pnr>Atg1*^{RNAi} side lagged behind the
208 other side by an average of about 25 µm, a reproducible, significant, and large reduction in
209 wound closure when syncytia formation was reduced (Figure 4E). These results suggest that
210 syncytia speed wound closure. It is difficult, however, to disentangle the roles of autophagy and
211 syncytia in this experiment, as the *Atg1* knockdown cells may move more slowly because they
212 are defective in the essential cellular function of autophagy and/or lacking syncytia. To address
213 this question, we found a strong correlation between the size of the cell/syncytium and the
214 distance it had moved from the start, measured at the time when the wound was half-closed.
215 This correlation was true for cells/syncytia in control wounds as well as for those when *Atg1* was
216 knocked down (Figure 4F,G respectively). These data indicate that syncytia formed through cell
217 fusion speed wound closure.
218
219 **Syncytia outcompete mononucleate cells at the leading edge of repair.**
220 To understand this phenomenon better, we further investigated control wounds. Because
221 about half the cells fused to form syncytia around wounds, we were able to compare the behavior
222 of syncytial to non-syncytial cells within the same wound, providing a well-controlled

223 environment for assessing how syncytia contribute to wound closure. In live imaging, we
224 observed that syncytia frequently moved faster than mononucleated cells toward the wound,
225 overtaking unfused cells as the wound closed. Figure 5A tracks four GFP-labeled cells near a
226 wound, with cell 1 furthest from and cell 4 closest to the wound (Figure 5A[i]). Middle cells 2 and
227 3 fuse with five others into a large syncytium, which advances toward the wound faster than both
228 non-fusing cells, and by 400 min after wounding the syncytium extends well beyond the unfused
229 cells (Figure 5A[iii]). This behavior was evident even without GFP labeling: Figure 5B-C show a
230 group of cells at the leading edge of the wound (the wound is recognized by the lack of p120ctn).
231 At 90 min after wounding, this region of the leading edge comprises three mononuclear cells
232 flanked on either side by syncytia (outlined in yellow); the middle of the three mononuclear cells
233 is outlined in orange (5B) and white (5C). By 150 min, the syncytia have pushed out all three
234 mononuclear cells from the leading edge, and at 360 min two of these mononuclear cells are
235 visible about 20 μm back from the wound edge. Indeed, we observed that several hours after
236 wounding, the entire leading edge was occupied by syncytia. To investigate how syncytia came
237 to occupy this position at the front lines of wound healing, we expressed MyoIIGFP/Zip-GFP,
238 which along with actin forms the contractile purse string and makes the leading edge visible,
239 along with p120ctnRFP to label cell borders. We analyzed the persistence of all mononuclear
240 and syncytial cells at the leading edge over the course of closure for three wounds, starting when
241 the leading edge was first visible about 30 min after wounding (Figure 5D-G). At the start, 75%
242 of the perimeter was occupied by syncytia with the rest occupied by 10-13 mononuclear cells
243 (Figure 5D). As the wound closed, the syncytia became larger and displaced all the mononuclear
244 cells, with the last mononuclear cell removed from the leading edge 20-160 min before closure

245 (Figure 5E-G). No mononuclear cell persisted at the leading edge through wound closure,
246 indicating that syncytia outcompete unfused cells to close the wound.
247
248 **Radial border fusion reduces intercalation, the rate-limiting step of wound closure**
249 Why do syncytia move faster? To address this question, we considered the geometry of
250 fusion because different fusion orientations could provide different benefits for wound repair.
251 We observed that fusions sometimes occur between two adjacent cells equidistant from the
252 wound, as diagramed in the top panel of Figure 6A and exemplified in Figure 1I^{iii}-I^{iv} (cells 1,2).
253 This breakdown of a radial border produces a syncytium elongated along the wound edge.
254 Alternatively, fusion may occur between adjacent cells at different distances from the wound, as
255 diagramed in the lower panel of Figure 6A and exemplified in Figure 1F (cells 3,4). This
256 breakdown of a tangential border produces a spoke-like syncytium pointing into the wound. To
257 analyze the frequency and timing of these two different axes of fusion, we calculated the
258 orientations of all lost borders in four wounds. (The angle of the lost border can be determined
259 for border breakdowns; it is difficult to determine for apical shrinking because the other fusion
260 partner is hard to identify). In four analyzed wounds, we identified 235 border breakdowns: 39
261 radial borders and 196 tangential borders (Figure 6B). Thus, there were about five-fold more
262 tangential borders lost to fusion than radial. Nonetheless, the two types had similar temporal and
263 spatial distributions around the wounds (Figure 6—figure supplement 1).
264 As a wound closes, fewer cells can occupy the ever-smaller leading edge, necessitating a
265 rearrangement of cell adhesions to allow cell intercalation, as depicted in the top of Figure 6C.
266 Indeed, when cells do not fuse after wounding, as in *Drosophila* wing discs, the impact of
267 intercalations on tissue fluidity is known to be a rate-limiting step of wound repair (Tetley et al.,

268 2019). As shown in the bottom of Figure 6C, the requirement for cell intercalation would be
269 reduced specifically by radial border fusion.

270 To consider the contribution of radial border fusions to wound closure, we took three
271 approaches. First, we analyzed existing data from the three wounds shown in Figure 5D-G, and
272 asked how many leading-edge cells fused radially vs. intercalated: 17-41% of cells removed
273 from the leading edge were removed through fusion, reducing the burden of intercalation
274 substantially (Figure 6D). Interestingly, the larger the percentage of cells that fused rather than
275 intercalated, the faster the wound closed (Figure 6D).

276 Second, we analyzed tissue fluidity as measured by the cell shape index, $\rho = P/\sqrt{A}$,
277 where P is cell perimeter and A is cell area. This dimensionless index characterizes the cell
278 jamming transition in vertex models of epithelia: for $\rho < 3.81$, a modeled isotropic epithelium is
279 in a jammed state with energy barriers that limit intercalations, giving rise to a solid-like tissue;
280 but for $\rho > 3.81$, the energy barriers vanish, yielding an unjammed fluid-like tissue (Bi et al.,
281 2016; Park et al., 2015). In real epithelia, the solid-fluid transition may take place at different
282 values of ρ (Wang et al., 2020), but higher ρ still implies greater tissue fluidity. We segmented
283 images of the pupal notum before and after wounding and calculated the distributions of cell
284 shape index for both syncytia and non-syncytial cells (Figure 7A-B). The mean cell shape index
285 increased significantly after wounding with syncytia having a higher shape index than nearby
286 post-wound non-syncytial cells ($p = 0.001$) and both having higher shape indices than pre-wound
287 cells ($p < 10^{-6}$). The post-wound epithelium is thus substantially more fluid-like than it was
288 before wounding

289 Third, we adapted the computational vertex model from Tetley et al. (2019) to include
290 probabilistic cell-cell fusions to directly investigate the role of cell fusion in tissue fluidity and

291 wound closure. We generated four initial cell configurations with similarly sized wounds and
292 used these to run four matched pairs of simulations – one that proceeded to close without any
293 cell fusions and the other that allowed fusions to occur with spatiotemporal probabilities that
294 matched our experimental observations (Figure 6B, Figure 6—figure supplement 1A). On
295 average, the probabilistic fusion-allowed simulations had 68 ± 14 (mean ± SD) fusions and
296 closed the wound in about 1/3 less time than those without fusions (Figure 7C). Selected frames
297 from one of the matched simulation pairs are shown in Figure 7D-E and full videos of this pair
298 are available as Video 5. Importantly, the modeled syncytia had no special properties: same
299 contractility as other cells, same target shape index, and same target area as the sum of the fused
300 pair. Just the presence of these larger cells reduced the need for intercalations during wound
301 closure and thus sped up the process.
302

303 **Tangential border fusions allow resources from distant cells to be mobilized to the wound**
304 **edge.**

305 In contrast to radial border fusions, tangential border fusions might provide a way for
306 cellular resources that would be trapped in distal cells to move toward the wound to contribute to
307 closure. To test this hypothesis, we generated small flip-out clones expressing actin-GFP and
308 wounded such that unlabeled cells intervened between the labeled cell and the leading edge
309 (Figure 8). Like cytoplasmic GFP in Figures 1I and 2C, we observed actin-GFP to equilibrate
310 between cells soon after fusing. For syncytia that did not have access to the leading edge (n =2),
311 actin-GFP levels remained uniform (Figure 8A,B). In contrast, syncytia with access to the
312 leading edge (n = 10) first uniformly distributed actin (Figure 8C^{ii}), but once the leading edge
313 was contacted, they redistributed actin-GFP to it (Figure 8C,D). Kymographs of actin-GFP

314 confirm that regardless of location, actin equilibrates between fusing cells within 5 minutes
315 (Figure 8B[iii], D[iv]); however, nearly all actin that originated in the distal cell is redistributed to the
316 leading edge in a syncytium positioned there (Figure 8D[iv]). In one striking instance, actin-GFP
317 appeared to travel through three cells to arrive at the leading edge from its initial location three
318 rows back (Figure 8E-G, Video 6). Importantly, although actin is labeled from only one of the
319 fusing cells, it likely represents the location of actin from all fusing cells, explaining why
320 syncytia are better able to occupy the leading edge. We envision that other resources would also
321 be concentrated in subcellular regions as needed by syncytia. This ability of syncytia to
322 concentrate pooled actin to the leading edge may allow syncytia to outcompete their smaller
323 mononuclear neighbors and close wounds more rapidly.

324 **DISCUSSION:**

325 Previous work established that polyploid cells – both cells with multiple nuclei and cells
326 with enlarged nuclei – are important for closing epithelial wounds in post-mitotic tissues (Losick
327 et al., 2013). Here we have used live-imaging to analyze the response to wounds of a diploid
328 mitotic tissue, the epithelial monolayer of the pupal notum. We found that syncytia form around
329 wounds by cell fusion at a remarkably high rate, with almost half the epithelial cells within 5
330 cells of the wound fusing with neighbors over the course of hours. Syncytial size increases with
331 wound size, indicating syncytia formation is a dynamic and scalable response to wounding.
332 Several lines of evidence demonstrate that syncytia are faster at closing wounds than unfused
333 cells. Knockdown of the autophagy gene *Atg1* reduces fusion around pupal wounds as was
334 previously reported for larval wounds; *Atg1* knockdown also reduces the rate of wound closure.
335 In both *Atg1* knockdowns and in controls, there was a consistent observation that the bigger the
336 syncytium, the faster it moved. Within control wounds, syncytia completely displace unfused
337 cells of the same genotype at the leading edge of the wound, such that wounds are closed entirely
338 by syncytia, even though there is a smaller number of syncytia than unfused cells. Finally,
339 computational modeling of wound closure with and without cell fusion shows that wounds with
340 fusion-based syncytia close faster because of the reduced need for cell intercalations.

341 Thus, wound-induced polyploidy is a generalized strategy for wound closure, used by
342 both mitotic and non-mitotic tissues. Although one might have wondered if polyploidy was a
343 wound response limited to tissues that cannot use mitosis to increase nuclear content, both
344 endoreplication and cell fusion into syncytia occur after wounding in this mitotically active
345 diploid tissue (Wang et al., 2015; White et al., 2024; this study). The requirement for *Atg1* for
346 fusion in both polyploid larval tissue and in diploid pupal tissue suggests that the fusion

347 mechanisms are common, despite the altered cell cycle of the starting cells. Further, our finding
348 that larger syncytia travel faster suggests that syncytia – and by extension perhaps cell
349 enlargement via endoreplication –occur as adaptations to close wounds faster.

350 We identified two unique properties of syncytia that may improve their wound-closing
351 ability. First, syncytia are larger than neighboring diploid cells and their presence enhances tissue
352 fluidity. Previous studies have determined that the rate-limiting step in epithelial wound healing
353 is the process of cell intercalation or rearrangement (Tetley et al., 2019). As the wound closes
354 and the leading edge encircling the wound gets smaller, fewer cells can occupy the leading edge.
355 The cells leaving the leading edge must remodel their cellular junctions, requiring time and
356 energy. Overall, tissue solidity slows closure, so enhancing fluidity promotes faster closure. By
357 fusing into larger syncytia, cells reduce the need for adhesion remodeling and intercalation and
358 instead just change shape as the leading edge becomes smaller. Moreover, the resulting larger
359 cells can have significantly more fluidity and less epithelial tension than their diploid
360 progenitors, as recently demonstrated in syncytia formed by age-induced epidermal cell fusion
361 (Dehn et al., 2023). As our computational modeling demonstrates, fusion can speed wound
362 closure by ~33% even when the resulting syncytia have no special properties besides being
363 larger than neighboring diploid cells. Making the syncytia individually more fluid would be
364 expected to speed closure even more.

365 The second unique property of syncytia is their ability to pool and concentrate the cellular
366 resources of the many constituent cells into a subcellular location within the large syncytium. We
367 explored this concept by monitoring the localization of actin within syncytia. Actin is important
368 for wound healing, as epithelial wounds close through the action of two actin-dependent
369 processes: the cinching of a multicellular actin cable at the leading edge that surrounds the

370 wound, sometimes called a purse string (Abreu-Blanco et al., 2012; Bement et al., 1993; Martin
371 and Lewis, 1992; Tamada et al., 2007), and the protrusion of actin-rich projections into the
372 wound (Abreu-Blanco et al., 2012; Farooqui and Fenteany, 2005). Pupal wounds have been
373 shown to use both processes, with the actin cable developing early and actin protrusions
374 appearing later in wound closure (Antunes et al., 2013). By labeling actin in individual cells
375 (clones), we were able to follow it redistribution in syncytia after fusion. As expected, at first
376 labeled actin diffuses and equilibrates throughout the new large cell. Remarkably however, when
377 the syncytium is in contact with the leading edge, labeled actin is concentrated at the leading
378 edge, even if the actin originated several cells away from the leading edge. Without fusion, the
379 labeled actin would have been trapped in a distal cell without access to the leading edge, but after
380 fusion, the syncytium can concentrate the actin of its many component cells at the wound front.
381 If N represents the number of cells that fused, our results suggests that syncytia can apply up to
382 N times more actin to the leading edge; considering that we observed syncytia with dozens of
383 nuclei, this could represent a significant enhancement of actin at the leading edge. Increased
384 actin might explain the ability of syncytia to outcompete diploid cells at the leading edge.
385 Presumably, other resources such as mitochondria and ribosomes could also be pooled and
386 concentrated by syncytia at cellular locations where they promote wound healing. It is known
387 that mitochondrial fragmentation is localized to the site of cellular injury (Horn et al., 2020), and
388 that ribosomes are localized at the tips of severed neurons (Noma et al., 2017), and syncytia
389 would have access to a larger pool of mitochondria and ribosomes than their component cells. By
390 pooling the cellular resources of component cells, syncytia may also allow lethally damaged cells
391 to survive by providing them with needed survival factors originating in cells further from the
392 wound. Thus, the concept of resource sharing that we demonstrate with actin may have

393 ramifications for many resources. Interestingly, it has been demonstrated that wound-induced
394 endoreplicating cells also increase protein levels of some wound-repair resources, such non-
395 muscle myosin, presumably possible because of the many copies present in the polyploid
396 genome (Losick and Duhaime, 2021).

397 Two visibly distinct cellular behaviors attended fusion in the apical plane of the adherens
398 junctions: border breakdowns and apical shrinking. Both processes were confirmed as fusion by
399 expressing GFP in clones and analyzing GFP sharing at fusion. Border breakdowns occurred
400 sooner after wounding than apical shrinking and appeared to be a faster process, as apical
401 shrinking started later and took hours to complete. It is unclear whether these differences in
402 appearance and timing indicate different mechanisms, as both require the autophagy gene Atg1.
403 For border-breakdown, it is simple to envision that fusion initiates near the apical adherens
404 junctions, which are under more tension than the basolateral membranes, and this may explain
405 why fusion proceeds more quickly there. We recently found that although epithelial tension
406 drops after laser wounding, it is restored within about 10 min (Han et al., 2023), consistent with
407 the timing of apical border breakdown. Also consistent with this model, in the *C. elegans*
408 hypodermis, developmental cell fusion has been observed to initiate at the apical side and travel
409 in the apical-to-basal direction (Mohler et al., 1998). It is also possible that fusion initiates at a
410 more basal site, and that fusion proceeds apically, with adherens junction disassembly occurring
411 later. Regardless of the site of fusion initiation, fusion seems to be a relatively equal process
412 when border breakdown is observed, with the resulting syncytium occupying the same footprint
413 that the two fusion partners did, at least initially. For apical shrinking, however, one cell appears
414 to transfer its cytoplasmic contents and nucleus into another recipient cell, with both cytoplasm
415 and nucleus moving laterally to the location of the fusion recipient, while the apical surface of

416 the donor cell shrinks. It is possible that apical shrinking may indicate a different location for the
417 initial fusion pore below the plane of the adherens junctions; it is also possible that this may
418 reflect a difference in the starting pressure of the two fusion partners, so that one subsumes the
419 other.

420 It is unclear what triggers either border breakdown or apical shrinking fusion. Many
421 developmentally programmed cell fusions are mediated by fusogens, cell surface proteins that
422 bring opposing membranes into close contact with each other, as in the *C. elegans* hypodermis
423 (Chernomordik and Kozlov, 2008; Iosilevskii and Podbilewicz, 2021; Markvoort and Marrink,
424 2011; Mohler et al., 2002; Podbilewicz et al., 2006; Sapir et al., 2007; Shemer et al., 2004). For
425 other cell fusions, the fusogen is elusive and may not exist, as none has been identified yet in
426 *Drosophila* myoblast fusions, which occur when a fusion competent myoblast generates actin-
427 rich podosome-like membrane protrusions that invade a founder cell (Kim et al., 2015b; Lee and
428 Chen, 2019; Petrany and Millay, 2019; Rushton et al., 1995; Sens et al., 2010). Wound-induced
429 fusion may be a response to the plasma membrane damage that occurs around wounds; indeed,
430 plasma membrane damage has been documented around both laser wounds and puncture wounds
431 (McNeil and Steinhardt, 2003; Shannon et al., 2017). Interestingly, in the large syncytial cells of
432 the *C. elegans* hypodermis, plasma membrane repair after a puncture wound requires the fusogen
433 EFF-1 (Meng et al., 2020).

434 Polyploidy as a wound response has begun to get increased recognition. In adult
435 *Drosophila,* epithelial puncture wounds are repaired by both endoreplication and syncytia
436 formation (Bailey et al., 2020; Besen-McNally et al., 2021; Grendler et al., 2019; Losick, 2016;
437 Losick et al., 2013; Losick et al., 2016). In the zebrafish epicardium, genetic ablation is repaired
438 by a wavefront of multinucleated polyploid cells formed by endomitosis, and these lead diploid

439 cells to encompass the heart (Cao et al., 2017). In adult mammalian cardiomyocytes, polyploidy
440 may be an adaptive response to maintain growth after the cardiomyocytes lose their ability to
441 complete mitosis. Mouse cornea endothelial cells endoreplicate to increase polyploidy to restore
442 tissue ploidy following genetic ablation (Losick et al., 2016). Mammalian hepatocytes are known
443 to become increasingly polyploid with age (Carriere, 1969; Wheatley, 2008) and in response to
444 various types of injury and disease (Gentric et al., 2015; Madra et al., 1995; Muramatsu et al.,
445 2000; Sigal et al., 1999; Toyoda et al., 2005; Wilkinson et al., 2019). All mechanisms that
446 promote polyploidy – fusion, endomitosis, endoreplication – result in larger cells with the
447 potential to localize more resources; of these, fusion would act the fastest after wounding
448 because there is no need for DNA replication. Interestingly, in *Drosophila* embryos, wounds
449 induce the surrounding cells to become larger by increasing their volume alone and not their
450 ploidy (Scepanovic et al., 2021), suggesting that simply an increase in size is important.
451 Although many examples of wound-induced polyploidy exist, it is still likely to be an
452 underreported phenomenon, as endpoint analysis might miss a transient polyploid response to
453 injury; live imaging is the surest way to identify a polyploid wounding response.
454 Another polyploid response to injury can occur after surgical implantation of biomaterials
455 for the purpose of guiding regeneration, as reviewed previously (Al-Maawi et al., 2017). In some
456 cases, only mononuclear cells of the immune system respond to the implant, and in these cases
457 the biomaterial is integrated into the body; in other cases, the implant triggers the fusion of
458 immune cells into multinucleated giant cells, and in these cases the material is degraded and
459 rejected. These multinucleated giant cells seem to share properties with the syncytia of the pupal
460 notum, as they are formed by fusion in response to an environmental trigger and they have an
461 aggressive ability to protect the animal in response to wounding. As these studies highlight,

462 understanding the formation, maintenance, and regulation of polyploid cells may improve our
463 ability to successfully implant biomaterials to aid tissue regeneration.

464 It is often noted that wound responses are similar to cancer cell behaviors. This similarity
465 extends to wound-induced syncytia and their counterparts, polyploid giant cancer cells, as both
466 cell types are highly aggressive and invasive. Chemotherapeutics induce the formation of
467 polyploid giant cancer cells (Illidge et al., 2000; Mosieniak et al., 2015; Ogden et al., 2015;
468 Wang et al., 2013), and some studies indicate that they can form through cell-cell fusion in
469 tumors (Melzer et al., 2018; Noubissi et al., 2015; Powell et al., 2011; Song et al., 2021; Zhang et
470 al., 2021). Once formed polyploid giant cancer cells are hypothesized to escape further
471 chemotherapy treatments due to increased resistance to genotoxic stress (Weihua et al., 2011).
472 These polyploid giant cancer cells and their progeny also exhibit increased migration and
473 invasion potential (Qu et al., 2013; Zhao et al., 2021). The parallels between the behaviors of
474 polyploid giant cancer cells and the wound-induced syncytia of the pupal notum highlight the
475 importance of understanding wound induced syncytia formation in a highly reproducible system,
476 as a basic understanding of how these cells form in the *Drosophila* notum could inform how they
477 become dysregulated in cancer.

478

479 **FIGURE LEGENDS:**

480 **Figure 1. Wounds induce epithelial syncytia via cell fusion.**

481 **A)** Syncytia form within 2 h post wounding, evident by the clustering of multiple nuclei within
482 cell borders.

483 **B)** The number of nuclei per syncytia increases over time after wounding. Number of nuclei was
484 estimated based on area and nuclear density (see text) for the 3 largest syncytia of 3 different
485 wounds, mean and SD.
486 **C-D)** Larger wounds generate larger syncytia. Images are at 3 h post wounding, single syncytium
487 outlined.
488 **E)** Syncytial apical area is proportional to initial wound size. Each dot represents a wound, made
489 with either low or high laser energy as sown. For each wound, the mean area of the three largest
490 syncytia is plotted. Bars represent SD.
491 **F)** A time course of six cells fusing within 30 min after wounding. Apical borders are lost (white
492 arrowhead) as syncytia form. Original cells are numbered.
493 **G)** All borders lost to cell fusion (white) mapped to cells in the first frame after wounding. The
494 leading edge of wound closure will form at dashed line; cells within the shaded area were
495 damaged by the wound and will be dismantled.
496 **H)** Distance from the wound center vs time for all border breakdowns in 3 wounds. Each symbol
497 represents a cell border. Leading-edge locations indicated by solid lines.
498 **I)** Cytoplasmic GFP is expressed in cell 1 before wounding and mixes with neighboring cells 2-4
499 by 2 min after wounding. Cytoplasmic sharing is followed by the lagging fusion indicator of
500 visible border breakdown (white arrow). The fates of cells 3 and 4 are shown at later times in
501 Figure 2D. Maximum intensity projections in A, C-D, G; single Z slices in F, I. Scale bars:
502 A,C,D,G = 20 μm, F,I = 10 μm. W and red star indicate wound.
503
504 **Figure 2: Cell fusion often appears as apical shrinking.**
505 **A)** The apical footprint of an epithelial cell shrinks in the epithelial plane after wounding (yellow
506 arrow).

507 **B)** Same sample as A, showing that the nucleus (asterisk) of the apically shrinking cell enters a
508 neighboring syncytium, outlined in B^{iv}.
509 **C)** Cell 1 expresses actin-GFP before wounding. After wounding, cell 1 fuses with cells 2-6
510 evidenced by GFP sharing, then the apical surface of cell 1 shrinks.
511 **D)** Two cells undergoing apical shrinking are identified in the X-Y plane with white and yellow
512 arrows, shown at three times after wounding. Below, two X-Z projections are shown for each, at
513 Y1 and Y2 as indicated, with the Z-plane of the adherens junctions (Z_{AJ}) indicated by dotted
514 lines. Rather than extrude, cytoplasm moves to the right as the cell depth in the Z-axis
515 diminishes, so that cytoplasm joins with the neighboring wound-proximal syncytium. These
516 video frames are a continuation of the sample shown in Figure 1I.
517 **E)** All cells displaying apical shrinking mapped to first frame after wounding.
518 **F)** All apical shrinking and border breakdowns were tracked in 3 wounds. Border-breakdown
519 fusions happen sooner after wounding than apical-shrinking fusions. A, B, C, D (top), and E
520 show maximum intensity projections. Lower panels in D show X-Z projections. Scale bar for all
521 panels A and B shown in $B^{iv.}$ A, B, C, D (top),E = 10 µm; D (X-Z projections) = 5 µm.
522
523 **Figure 3: Half the cells near the wound fuse to form syncytia, demonstrated by tracking**
524 **individual cell fates.**
525 **A)** All GFP labeled cells in the region of fusion (80 µm) were tracked in 5 wounds over 6.5 h
526 after wounding to determine frequency of fusion initiation (GFP mixing) and later morphological
527 changes into syncytia. All morphological fusion events were preceded by GFP sharing, and 90%
528 of GFP sharing events were followed by morphological fusion. Untrackable cells lost GFP, see
529 Figure 3—figure supplement 1A.

530 **B-C)** Pre-wound location of persisting and fusing cells from panel A is shown with respect to the
531 wound center. Panel B shows that fusion is common within 70 µm. Panel C shows that apical-
532 shrinking fusion and border-breakdown fusion occur at similar distances from the wound.
533
534 **Figure 4: *Atg1* promotes wound-induced fusion and faster wound closure.**
535 **A)** Overview: *Atg1* was knocked down in central *pnr* domain (pink), visualized by nls-mCherry
536 (not shown). A laser pulse was targeted to the edge of the *pnr* domain (right or left) so that the
537 wound extended into both *Atg1* knockdown and control domains, allowing the symmetry of
538 response to be analyzed.
539 **B-C)** Inhibition of *Atg1* decreased the frequency of wound-induced fusion in the *pnr* domain. For
540 border loss, n = 11 pupae, $p < 0.0001$. For apical shrinking, n=9 pupae, $p = 0.0008$ (paired T-
541 test).
542 **D-E)** Wound closed more slowly when *Atg1* was knocked down. (D) Radius of the wound was
543 calculated by the distance between the wound center and the leading edge in *pnr* or control
544 domains. (E) Difference in the wound radius between *pnr* and control domains over time (i.e.,
545 wound asymmetry) is shown. Each dot represents one wound. With no genetic manipulation in
546 either domain (black), wound radius was slightly larger in *pnr* than in control domain. When
547 *Atg1* was knocked down in the *pnr* domain, the asymmetry grew over time indicating slower
548 wound closure on the *Atg1* knockdown side. $p = 0.0031$ (5 hr) calculated from two-way
549 ANOVA, fit full model, comparing each cell mean with the other cell mean in that row. error bar
550 = 1 +/- SEM.
551 **F-G)** Larger cells (*i.e.* syncytia) move further during wound closure, evident in control wounds
552 (F) or with *Atg1* knockdown (G). Each data point represents a cell or syncytium present at the

553 leading edge when the wound is half closed. The curve of square root area was overlaid for
554 comparison, as it represents the amount of movement expected based on reshaping of a
555 cell/syncytium from an initial round state to one strongly elongated towards the wound.
556
557 **Figure 5: Syncytia outpace mononuclear cells.**
558 **A)** Before wounding, two clusters of cells are labeled with GFP, 1-2 and 3-4 (white numbers).
559 After wounding, cells 2 and 3 fuse with neighbors 5-9 to form a syncytium (dashed leading edge
560 in A^{iii}), which advances toward the wound, passing unfused cell 4 (arrow).
561 **B-C)** Unfused cell (outlined in orange and white) is replaced at leading edge by neighboring
562 syncytia (S and yellow outline).
563 **D)** Leading-edge perimeter was analyzed over time for three wounds, also analyzed in panel G.
564 Percent leading edge occupied by syncytia increased over time to 100%.
565 **E)** Images of sample 1 from graph D. Unfused cells (arrows) were tracked over the course of
566 wound closure; 30 min after wounding, 10 unfused cells at the wound leading edge are indicated
567 by arrows.
568 **F)** At 120 min, the last unfused cell was ejected from leading edge (arrow). The wound closed at
569 140 min.
570 **G)** The loss of unfused cells was analyzed over time in the three wounds from panel D. All
571 unfused cells are excluded from leading edge by syncytia well before each wound closed 20-160
572 min later.
573 Images are single Z slices in A^{i}-A^{ii} and maximum intensity projections in A^{iii}-F. Scale bar for
574 B,C shown in C^{iv} and for E,F shown in F. Scale bars in A,E,F = 20 μm, B,C = 10 μm.
575

576 **Figure 6: Cells fuse along different axes at different frequencies, reducing the number of**
577 **wound-proximal cell intercalations.**

578 **A)** Illustration of tangential vs radial border breakdown. **B)** More tangential than radial borders
579 break down after wounding. Data are from four wounds, with a total of 235 border breakdowns:
580 39 radial and 196 tangential. Individual counts are shown per wound with mean and SEM. **C)**
581 Fusions across radial borders reduce intercalation at a wound. **D)** Quantification of intercalations
582 and fusions around the three wounds of Figure 5D,G.
583

584 **Figure 7: Computational modeling indicates that fusion speeds the rate of wound closure**
585 **because of reduced cell intercalation.**
586 **(A-B)** Experimental observations of cell shape index (perimeter divided by square root of area).
587 By two hours after wounding, the cell shape index has increased for both syncytia and non-
588 syncytial cells within two rows of the wound margin. These increases indicate an increase in
589 tissue fluidity. (A) Cells and syncytia were segmented, and cell shape index calculated, as shown
590 for this image at 115 min after wounding; cell shape index indicated by color-coding. (B) Pre-
591 and post-wound cell-shape distributions were compiled from 6 pupae. The red dashed line
592 represents the critical cell shape parameter, 3.81, for the solid-to-fluid transition in vertex models
593 of epithelia. Grey boxes span the interquartile range with a line at the median; whiskers extend
594 out 1.5x the median-to-closest-quartile range; and outliers beyond the whiskers are plotted as
595 individual points. Distributions include 1304 pre-wound mononucleate cells, 168 post-wound
596 mononucleate cells, and 52 post-wound syncytia; **** denotes $p < 10^{-6}$ level; *** denotes $p <$
597 0.001.

598 **(C-E)** Vertex model simulations of wound closure with cell fusion allowed or suppressed. When
599 the spatial and temporal probabilities for cell fusion match experimental observations, the model
600 yielded 55 ± 22 fusions per wound (mean ± standard deviation), with 15 ± 6 of these occurring at
601 radially aligned edges. As shown in C, fusions in the model speed wound closure: four
602 simulations per condition; shaded regions denote standard deviation; time normalized to the
603 average time to closure when fusion is suppressed. Panels D-E show a series of still frames from
604 a matched pair of simulations in which fusion is allowed or suppressed. Corresponding videos
605 are available as Video 5.
606
607 **Figure 8: Syncytia concentrate pooled resources at the leading edge.**
608 Random scattered cells expressing Actin-GFP were generated by heat-shock mediated flip-out
609 expression of Gal4. **A-B)** Labeled actin is expressed in cell 1 before wounding (A^{i},B^{i}). These
610 cells are not close to the wound (inset in A^{ii}). By 28 min after wounding, actin-GFP equilibrated
611 between cells 1 and 2 (A^{ii},B^{ii}), demonstrating cytoplasmic fusion. The resulting syncytium had
612 no access to the leading edge, and actin remained equilibrated, as shown in the kymograph (B^{iii})
613 generated from actin-GFP intensity over time at the yellow line in B^{ii}. Fusion was confirmed at
614 180 min after wounding by apical shrinking of cell 2 (not shown). **C-D)** Labeled actin is
615 expressed in cell 1 before wounding (C^{i},D^{i}) and equilibrates between cells 1 and 2 by 6 minutes
616 after wounding, demonstrating cytoplasmic fusion (C^{ii},D^{ii}). The resulting syncytium contacts the
617 leading edge, and by 28 min after wounding actin from cell 1 is redistributed to the wound
618 margin (C^{iii},D^{iii}), as shown in the kymograph (D^{iv}) of actin intensity over time at the yellow line
619 in D^{iii}. Fusion was confirmed at 55 min after wounding, by apical shrinking of cell 1 (not
620 shown). **E-F)** Before wounding, actin-GFP in cell 1 is three cells away from the future leading

621 edge. After wounding, fusion of cells 1-4 allows actin-GFP to be subcellularly localized to the
622 leading-edge actin cable. Border breakdown is visible between cells 1-2 at 30 min after
623 wounding (E^{v}) and apical shrinking occurs later (see Video 6). **G)** Mean profile plot of actin-
624 GFP comparing the syncytia in F^{v} at 30 min after wounding (dark line) with the cells in F^{i} before
625 wounding (dotted line) demonstrating that nearly all actin-GFP has been relocalized to the
626 leading edge from its starting position 20-30 µm away. Single Z slices for E^{i-ii}, F^{i-ii}; maximum
627 intensity projections for A-D, E^{iii-v}, F^{iii-v}. Scale bar for panels in A-B shown in B^{ii}, 10 µm. Scale
628 bar for panels in C-D shown in D^{iii}, 5 µm. Scale bar for panels E-F shown in F^{v}, 10 µm.
629
630 **Figure 1—figure supplement 1: Characteristics of the pupal notum epithelium.**
631 **A-C)** An example of mitosis occurring ~80 µm from the wound. Scale bar for A-C shown in C^{v},
632 10 µm. **D)** Z-slices at different depths of GFP-labeled cells reveal that the apical area (red
633 outline) does not reflect the position of cells at basal slices (yellow arrows). The nuclear shadow
634 in panel D^{ii} demonstrates the location of the nucleus. Scale bar, 10 µm. **E-H)** Ecad-GFP and
635 p120ctnRFP colocalize and behave similarly during border breakdown. Arrowheads in F-H
636 points to borders breaking down in first hour after wounding. Scale bar for F-H shown in H^{v}, 10
637 µm.
638
639 **Figure 3—figure supplement 1: Temporal analysis of fusion events**
640 **A)** An example of an untrackable cell is shown. After wounding, cell 1 loses cytoplasmic GFP,
641 but there is no obvious recipient cell. Cell 1 then shrinks. Scale bar = 10 µm.
642 **B)** Cells individually labeled with GFP reveal the timing and frequency of fusion or GFP loss
643 (untrackable). **C)** Fusion cells from panel B were divided into two types of fusion events,

644 shrinking cells and border breakdowns, to compare the temporal onset of each type of fusion. **D)**
645 Cell shrinking was a lengthy and variable process, lasting up to hundreds of minutes. 274
646 shrinking cell events from three wounds were identified by p120ctnRFP, mean and SD indicated.
647
648 **Figure 6—figure supplement 1: Comparisons of tangential and radial border breakdowns**
649 **A)** The distance of tangential and radial border breakdown events from the wound, compared
650 over time binned into 10 min intervals. The data is the same as in Figure 6B, from four wounds,
651 with a total of 235 border breakdowns: 39 radial and 196 tangential. Border breakdown events
652 were identified by p120ctn. B) The timing of tangential vs radial border breakdown fusion events
653 observed in single GFP-labeled cells.
654
655 **Video 1: Syncytial cells form after wounding in the *Drosophila* pupal notum.** Epithelial cell
656 borders in red (p120ctnRFP) and nuclei in green (HistoneGFP). White box on first frame denotes
657 field of view in Figure 1A. Video begins before wounding and extends to 2 h after wounding.
658
659 **Video 2: GFP mixing precedes border breakdown after wounding.** Arrow in first frame
660 points to cell border between cells that will fuse after wounding. GFP diffusion into the
661 unlabeled cell precedes visible border breakdown. w, wound region. Cell borders are labeled
662 with p120ctnRFP. Video begins before wounding and extends to 2 h 10 min after wounding.
663 Same cells as Figure 1I and 2D.
664
665 **Video 3: Shrinking cells contribute to syncytia.** Arrow in first frame points to an individual
666 cell labeled with Actin-GFP that fuses by shrinking after wounding. This cell contributes its

667 actin-GFP to neighboring cells minutes after wounding then shrinks much later; shrinking is first
668 evident about 1.5 h after wounding and is nearly complete by 3.5 h after wounding. w, wound
669 region. Cell borders are labeled with p120ctnRFP. Same cells as Figure 2C.
670
671 **Video 4:** Blood cells labeled with *hml-Gal4, UAS-GFP* were observed migrating to and along
672 the basal side of the wounded pupal notum. Video is a Z-stack maximum projection. Wound is
673 indicated by w in the first frame. No GFP was observed to enter the epithelium, indicating that
674 blood cells do not fuse with the wounded epithelium. Six similar wounds were analyzed, with no
675 evidence of fusion.
676
677 **Video 5**: Computational vertex models show that incorporating cell fusion speeds wound
678 closure. When fusion occurs with spatiotemporal and edge-orientation probabilities that match
679 experimental observations, wound closure in the model with fusion is 33% faster than when
680 fusion is suppressed.
681
682 **Video 6: Syncytia pool actin and concentrate it at the leading edge of repair.** An individual
683 cell labeled with actin-GFP fuses with wound proximal cells and contributes its actin to the
684 leading edge of the syncytium. w, wound region. The original source cell and its immediate
685 neighbor go on to shrink into wound proximal cells. Cell borders are labeled with p120ctnRFP.
686 Same cells as Figure 6E,F.
687
688 **Acknowledgements:** We thank James O'Connor for his original observations of syncytial cells
689 around pupal wounds, and Kimi LaFever Hodge for technical assistance, and we thank Chloe

690 Hecht and Kimi LaFever Hodge for comments on the manuscript. Stocks obtained from the
691 Bloomington Drosophila Stock Center (NIH P40OD018537) were used in this study. JSW was
692 supported by NIH T32HD007502 to Chris Wright, and JH was supported by American Heart
693 25PRE1374646 to JH. This work was supported by the National Institute of General Medical
694 Sciences R01GM130130 to APM and MSH.
695

696 **Resource availability**

697 **Lead contact**

698 Requests for fly lines, reagents, and additional questions should be directed to Dr. Andrea Page-
699 McCaw (andrea.page-mccaw@vanderbilt.edu)

700 **Materials availability**

701 Fly lines generated in this study are available from the Bloomington *Drosophila* Stock Center or
702 from the lead contact.

703 **Data availability**

704 All primary microscopy videos are available through OSF.

705 **Experimental model and subject details**

706 ***Drosophila melanogaster***

707 *Drosophila* lines used in this study are in Table S1. All *Drosophila* lines were maintained on
708 standard cornmeal-molasses media supplemented with dry yeast. All flies, except those used in
709 heat-shock flip clonal analysis, were raised at room temperature. For clonal analysis experiments
710 flies were raised at 18 degrees Celsius until the 3rd instar stage when they were heat shocked in a
711 circulating water bath at 37°C for 3 minutes. They were then allowed to develop at room
712 temperature to 15-18hr after puparium formation (APF) before wounding experiments (described
713 below) were conducted. To knock down *Atg1*, *Atg1*^{RNAi} was crossed to the stock for internally
714 controlled wounding analysis, expressing *Ecad-GFP* and *TubP-Gal80*^{ts} ubiquitously and *pnr-*
715 *Gal4, UAS-nls-mCherry* in the central region of the notum, similar to our previous system
716 (O'Connor et al., 2021b). Crosses were moved to 29° for 6 days to allow expression of the RNAi
717 construct and dissected between 12-15 hr APF.

718 **Method details**

719 **Pupal mounting**

720 At room temperature, white prepupae were identified and marked within plastic food vials. 15-18
721 APF pupae were removed from the vial onto a piece of double-sided tape (Scotch brand,
722 catalogue #665) applied to a microscope slide. Using fine forceps, the anterior pupal case was
723 removed exposing the head and notum of all pupae applied to the tape, as previously described
724 (O'Connor et al., 2022; Shannon et al., 2017). The tape was carefully removed from the
725 microscope slide and inverted onto a pre-prepared cover glass (Corning 2980-246, 24 mm x 64
726 mm) (O'Connor et al., 2022). The pupae were carefully pressed down onto the cover glass by
727 adhering the section of tape above the pupal head. Once the notum was visibly pressed onto the
728 cover glass an oxygen permeable membrane (YSI, standard membrane kit, cat#1329882) was
729 applied to prevent the pupae from drying out during imaging.

730 **Pupal survival**

731 Following imaging, pupae were kept mounted as described above and allowed to continue to
732 develop and eclose for 3-4 days. Pupae that continued developing until they were able to crawl
733 out of the partially dissected case were classified as 'survived' and their data acquired form these
734 samples were used for analysis. If a pupae did not survive to eclosion, the associated datasets
735 were not used in the study.

736 **Live imaging**

737 Images were collected using a Nikon Ti2 Eclipse with X-light V2 spinning disc (Nikon, Tokyo,
738 Japan) with a 40X 1.3 NA oil-immersion objective or 60X 1.4 NA oil-immersion objective.
739 Unless otherwise noted samples were imaged pre-wounding, immediately after wounding, every
740 2 min for 30 min, and then every 10 min for 6 h. Images were pre-processed in NIS-Elements
741 using combinations of background subtraction, rolling ball correction, local contrast, and

742 Denoise a.i. Assembly of figure panels was done using Affinity Designer and frames were
743 centered on the entity in focus, compensating for frame shift due to wounding.

744 **Laser ablation**

745 A single pulse of a 3rd harmonic (355 nm) Q-switched Nd:YAG laser (5 ns pulse-width,
746 Continuum Minilite II, Santa Clara, CA) was used for laser ablation. Laser pulse energies were
747 kept to 1.9 μJ +/- 0.1 μJ, increased from our previous report (O'Connor et al., 2021b) to keep the
748 wound size similar between old and new ablation rig.

749 **Border breakdown and tangential vs radial assignment analysis**

750 Individual border breakdown events were manually observed using FIJI by identifying syncytia
751 late in the video and back-tracking to determine which borders broke down to form each
752 syncytium. These borders were traced back to the first frame after wounding to develop the map
753 on Fig 1G. For each border breakdown event, distance from the center of the wound and time
754 after wounding were recorded in Microsoft Excel. These events were categorized as tangential or
755 radial based on the orientation of the border-to-be-lost relative to a vector pointing outward from
756 the center of the wound. Specifically, the line tool in FIJI was used to measure both the angle of
757 the border with respect to the horizon, θ, and the angle of the line from the center of the wound
758 to the center of the border with respect to the horizon, α. If $|\cos(\alpha - \theta)| \geq \cos 45°$, then the
759 border was classified as radial; otherwise, the border was classified as tangential.

760 **Shrinking cell initiation / duration analysis**

761 Shrinking cells were identified in live microscopy videos by beginning at the end of the video
762 and playing backwards in FIJI. Backwards, a shrinking cell appears to bloom from the epithelial
763 layer, characterized by the expansion of a bright puncta of p120ctnRFP. Each cell that underwent
764 this behavior was marked on a single frame of the video, then the distance from the center of the

765 wound when shrinking started was denoted as well as the time that the shrinking started and
766 completed. All cells that shrank were then manually traced back to the first frame after wounding
767 to develop the map of shrinking cells (Fig 2E).

768 **Approximating nuclei per syncytia**

769 Nuclei and cell borders do not align in Z-projections of the pupal notum as the cells are non-
770 prismatic. To estimate the number of nuclei per syncytium, the pre-wounding density of nuclei
771 per unit area was determined for the circular region where syncytia form after wounding. Next,
772 the apical area of the three largest syncytia/cells around a wound was measured at 0h, 1 h and 2 h
773 post wounding. The area of each syncytia was multiplied by the nuclear density to yield the
774 approximate number of nuclei per syncytia. The number of nuclei in each of the three syncytia
775 was averaged to give a value for each of three samples in Figure 1B.

776 **Measuring apical area of syncytia across varied wound sizes**

777 The three largest syncytia were determined by eye in FIJI for six samples, three ablated at 1.9 μJ
778 and three ablated at 3 μJ ablation. The apical area of syncytia was measured 3 h post wounding
779 using the p120ctnRFP signal. Initial wound size was calculated by measuring Myosin II marked
780 leading edge when it became apparent 30-160 min post wounding.

781 **Unfused cells at leading edge: count and percent analysis**

782 Unfused cells at the leading edge were identified using FIJI by a lack of border breakdowns.
783 Each unfused cell was manually observed over the duration of wound closure and the time at
784 which it departed from the leading edge was noted. A count of unfused cells at the leading edge
785 was created in Excel and formal graphs were generated using Prism 9. To measure percent of the
786 leading edge comprised of unfused vs. syncytial cells, each unfused cell's leading edge contact
787 was measured in FIJI using the polygon line tool. The total circumference of the wound was

788 measured using the polygon line tool and unfused cell measurements were subtracted from the
789 total to infer the syncytial occupancy at the leading edge. Formal histograms were generated
790 using Prism 9.

791 **Analyzing GFP labeled cells**

792 107 individually labeled GFP cells were analyzed across 5 wounds over 6.5 h. The position of
793 the ablation was optimized to place as many individually labeled cells within 40-80 μm from the
794 center of the wound as possible. After wounding it was possible to identify a mixing event by the
795 decrease in intensity from the source cell with a corresponding increase in intensity of a
796 previously unlabeled neighbor. Intensity differences made it possible to distinguish instances
797 where two source cells were adjacent to each other but only one had a mixing event. However,
798 large patches of source cells were not evaluated because inter-patch mixing was not
799 distinguishable. To evaluate if border breakdowns were preceded by mixing, the 11 individually
800 labeled cells that had border breakdowns were tracked back to the start of the video and
801 confirmed to have a mixing event. There was never an instance where a labeled source cell had a
802 border breakdown without a prior mixing event occurring.

803 **Wound closure analysis**

804 A pigmented scar forms at the site of laser ablation making identifying the exact moment a
805 wound is closed difficult. Since the scar is approximately the same size in each sample, the time
806 point at which the Myosin II signal disappeared below the scar was used as a proxy for closure.

807 **Fusion analysis**

808 A cell border was counted as a location of wound-induced fusion if it met three criteria: (1)
809 adherens junctions along the cell border were lost; (2) the lost adherens junctions were not
810 restored; and (3) the loss of adherens junctions was accompanied by a morphological change of

811 the neighboring cells, for example, the moving apart of tri-cellular junctions previously
812 connected by the lost cell border. Since border-breakdown fusions are observed most frequently
813 within 1 hr after wounding, we counted all such fusions occurring within 1 hr 40 min of
814 wounding.

815 When comparing the fusion frequency in *pnr* versus control domains, we used a
816 landscape-oriented rectangle centered on the wound with its height defined by the inner radius of
817 the zone of nuclear membrane damage visualized by the release of nls-mCherry from the
818 nucleus, which is approximately the same as the zone of lysis (O'Connor et al., 2021a).
819 Replacing the annular region with an extended rectangle excludes possible heterotypic fusions
820 along the *pnr*-control border just above and below the wound. To calculate the frequency of
821 fusion, in addition to the raw number of fusion borders, the total number of cell borders was also
822 estimated by area-based scaling of the border count within a randomly selected 60-x-60-pixel
823 (16.8-x-16.8-µm) region in the pre-wound image.

824 Since fusions can also appear as apical shrinking rather than border breakdown, we also
825 quantified the number of apical-shrinking cell fusions in *pnr* versus control domains. Apical-
826 shrinking cell fusions were defined as diploid cells that decreased in surface area over time and
827 fully disappeared within a 5-hr movie. As with fusion analysis, cells near the *pnr*-control border
828 were excluded. Apical shrinking cells were counted manually and their spatial locations marked
829 using FIJI's "Multi-point" tool.

830 **Determining the effect of syncytia on wound closure**

831 The distance between the leading edge and the wound center over time was used to calculate the
832 speed of wound closure. The distance was calculated using the coordinates of the wound center
833 and fixed points on the leading edge. To identify fixed positions on the leading edge that are

834 unbiased and consistent over time, four reference lines, all crossing the center of the wound,
835 were drawn using the red channel with only the nuc-mCherry signal: line 1 along the edge of the
836 *pnr* domain labeled by nuc-mCherry, line 2 perpendicular to line 1, and line 3
837 and 4 are 30˚ from line 2. These references lines were then overlaid on the green channel with
838 the E-cadherin signal.

839 To determine the speed of wound closure, the intersection of E-cadherin marked leading
840 edge and reference lines 2-4 were used as the position of the leading edge. That is, at each time
841 point, a total of 6 positions of the leading edge were recorded, among which 3 will be in the *pnr*
842 domain and the other 3 in the ctrl domain. The average distance (d) between the leading edge and
843 the center of the wound were calculated at each time point for both the *pnr* domain (d_{pnr}) and the
844 control domain (d_{ctrl}). The difference between control and *pnr* distance ($\Delta d = d_{pnr} - d_{ctrl}$) was
845 calculated over time for both the control pupae with no genetic manipulation in the *pnr* domain
846 (*pnr* > +) and experimental animals with *Atg1* knocked down in the *pnr* domain (*pnr* >
847 $Atg1^{RNAi}$). To determine whether Δd is statistically different between control and experimental
848 pupae at each time point, two-way ANOVA (fit using full model) was used, comparing each cell
849 mean with the other cell mean in that row.

850 To determine the distance syncytia covered during wound healing, syncytia were
851 analyzed (1) at the leading edge when wound is half closed and (2) within the bow-tie region
852 between reference line 3 and 4. ROIs were drawn along syncytia of interest using the "Freehand
853 selections" tool of FIJI. In addition to syncytia location when wound is half closed, the starting
854 position of cells that later fuse to form syncytia were also recorded in live-imaging videos,
855 tracking the syncytia back in time. In addition to area, the coordinates of ROIs outlining syncytia
856 at different time points were obtained using a self-written FIJI Macro. Within each ROI, the

857 coordinate closest to the center of the wound was recorded using python, as the location of the
858 syncytia. The distance a certain syncytium moved was calculated by subtracting the distance
859 between the syncytium and the wound center when the wound was half closed from the distance
860 between the syncytium and the wound center immediately after injury.

861 **Calculating intercalation in live imaging**

862 The change in the number of cells when the leading edge forms at 30 min (N_{start}) to when the
863 wound is closed (N_{end}) is equal to the number of intercalations plus the number of radial fusion
864 events. Thus, (intercalations = ΔN – radial fusions). For the same three samples used in Fig
865 4D,G, we determined ΔN from N_{start} at 30 min and N_{end} when the wound had closed. Radial
866 fusions were tallied by manually observing border breakdown events between the leading-edge
867 cells and intercalations were calculated. Each radial fusion was counted as one prevented
868 intercalation event.

869 **Calculating cell shape index**

870 Images of pupae labeled with Ecad-GFP were segmented into individual cells with Cellpose
871 (Stringer et al., 2021); cells that were not readily segmented were excluded from subsequent
872 analysis. To avoid perimeter inflation due to pixelation, the boundaries of segmented cells were
873 smoothed by taking the midpoint between every other pair of boundary pixels. Smoothing and
874 calculation of perimeters, areas and cell shape indices ($P/\sqrt{A}$) were performed in Mathematica
875 (Wolfram Research Inc., Champaign, IL).

876 **Vertex models with cell fusion**

877 Simulations of wound healing were run using vertex models implemented in Mathematica
878 (Wolfram Research Inc., Champaign, IL) following the methods of Tetley et al. (2019)and using
879 parameters that match experimental observations from the *Drosophila* pupal notum as detailed in

Han et al. (2024) with the following exceptions: the mean line tension on each edge (Λ) was specified in terms of a target shape parameter (ρ_0) such that $\Lambda = -2\rho_0\Gamma\sqrt{A_0}$, where the contractility (Γ) and target cell area (A_0) were taken from Han et al. (2024) and $\rho_0 = 3.745$ was chosen so that the actual cell shape index matched experimental pre-wound measurements; and the line tension variability (σ_m) was decreased from 1.0 x 10^{-2} to 9.3 x 10^{-4} so that the intercalation rate in unwounded cell sheets matched experimental observations. Pre-wound configurations were generated by performing a Voronoi tessellation of a circular area with 320 randomly distributed seed points and then equilibrating the cell configuration without stochastic fluctuations until it reached a steady state. Wounds were introduced by removing all cell borders within a circular patch ~8 cells across and removing the wound's contributions to the energy Hamiltonian. To handle wound closure and fusion, the following additions were made to the model: (1) purse-string tension on the leading edge of the wound was incorporated as in Tetley et al. (2019) with a normalized strength of 0.115; (2) traction/crawling forces of cells on the leading edge of the wound were incorporated as a uniform tensile stress acting inwardly on the edges and vertices of the wound area (similar to the uniform stress applied to the outer edge of the patch to represent tension from surrounding cells); this inward stress had a normalized strength of $\Sigma_{in}/KA_0 = 0.13$, where K is the area elasticity modulus; (3) the cell-cell interfaces at which fusion would occur were selected stochastically with probabilities that depended on time, distance from the wound, and the radial or tangential orientation of the interface – all chosen to match experimental observations reported here; and (4) the fusion of two cells was handled by eliminating the interface between those cells and setting the target area of the fused cell to the sum of the target areas of its two progenitors. All cells, fused or not, had the same contractility and target shape parameter.

903 **Kymograph and plot profile analysis**

904 Actin-GFP intensity was analyzed using the kymograph tool in FIJI after drawing a 11-pixel line
905 through the middle of the syncytia. Profile plot values were exported from NIS elements to Excel
906 and graphs were generated using Prism.

907

Key Resources Table				
Reagent type (species) or resource	**Designation**	**Source or reference**	**Identifiers**	**Additional information**
Fly line (*Drosophila melanogaster*)	"HistoneGFP"	BDSC:	24163	*w*; P{w^{+m} =His2Av-EGFP.C}2/ SM6a*
Fly line (*Drosophila melanogaster*)	"p120ctnRFP"	gift from Shigeo Hayashi (Ogura et al., 2018)		*y; ubiP-p120ctn-TagRFP*
Fly line (*Drosophila melanogaster*)	"Ecad-GFP"	Kyoto Drosophila stock center	109007	*w*; {w^{+}*=ubi-p63E-shg.GFP}5*
Fly line (*Drosophila melanogaster*)	"AyGal4"	BDSC:	3953	*w^{1118}; P{w^{+mC}=AyGAL4}25/CyO*
Fly line (*Drosophila melanogaster*)	"hsFLP"	BDSC:	55813	*w^{1118}; P{y$^{+t7.7}$ w^{+mC}=hs-FLPD5}attP2*
Fly line (*Drosophila melanogaster*)	"GFP"	BDSC:	1522	*w*; P{w^{+mC}=UAS-GFP.S65T}eg^{T10}*
Fly line (*Drosophila melanogaster*)	"Actin-GFP"	BDSC:	7310	*w^{1118}; P{w^{+mC}=UASp-Act5C.T:GFP}2; l(3)*/TM6C, Sb^{1} Tb^{1}*
Fly line (*Drosophila melanogaster*)	"MyosinII-GFP"	BDSC:	51564	*w*; P{w^{+mC}=PTTGC}zip^{CC01626}/SM6a*

Fly line (*Drosophila melanogaster*)	"HistoneRFP"	BDSC:	23651	*y w; His2AvRFP / CyO*
Fly line (*Drosophila melanogaster*)	"UAS-Atg1^{RNAi}"	BDSC	26731	*y^1 v^1; P{$y^{+t7.7}v^{+t1.8}$=TRiP.JF02273}attP2*
Fly line (*Drosophila melanogaster*)	internally controlled knockdown for wounding	this study		*w*; Ecad-GFP; pnr-Gal4, tub-Gal80^{ts}, UAS-nls-mCherry/SM6-TM6B*
Fly line (*Drosophila melanogaster*)	hml-Gal4	BDSC	30139	*w^{1118}; P{w^{+mC} =Hml-GAL4.Delta}2*
Software	FIJI	Schindelin et al., 2012	RRID: SCR_002285	
Software	NIS Elements	Nikon Instruments Inc.	RRID: SCR_002285	
Software	Microsoft Excel	Microsoft	https://www.microsoft.com/en-us/microsoft-365/excel	
Software	GraphPad Prism 9	GraphPad	https://www.graphpad.com/scientific-software/prism/	
Software	Affinity Designer	Affinity Serif	https://affinity.serif.com/en-us/designer/	

908

909 **REFERENCES**

910 Abreu-Blanco, M.T., Verboon, J.M., Liu, R., Watts, J.J., Parkhurst, S.M., 2012. Drosophila
911 embryos close epithelial wounds using a combination of cellular protrusions and an
912 actomyosin purse string. J Cell Sci 125, 5984–5997.

913 Al-Maawi, S., Orlowska, A., Sader, R., James Kirkpatrick, C., Ghanaati, S., 2017. In vivo
914 cellular reactions to different biomaterials-Physiological and pathological aspects and their
915 consequences. Semin Immunol 29, 49–61.

916 Alvarez-Dolado, M., Pardal, R., Garcia-Verdugo, J.M., Fike, J.R., Lee, H.O., Pfeffer, K., Lois,
917 C., Morrison, S.J., Alvarez-Buylla, A., 2003. Fusion of bone-marrow-derived cells with
918 Purkinje neurons, cardiomyocytes and hepatocytes. Nature 425, 968–973.

919 Antunes, M., Pereira, T., Cordeiro, J.V., Almeida, L., Jacinto, A., 2013. Coordinated waves of
920 actomyosin flow and apical cell constriction immediately after wounding. The Journal of
921 Cell Biology 202, 365–379.

922 Bailey, E.C., Dehn, A.S., Gjelsvik, K.J., Besen-McNally, R., Losick, V.P., 2020. A Drosophila
923 Model to Study Wound-induced Polyploidization. J Vis Exp.

924 Bement, W.M., Forscher, P., Mooseker, M.S., 1993. A novel cytoskeletal structure involved in
925 purse string wound closure and cell polarity maintenance. J. Cell Biol. 121, 565–578.

926 Besen-McNally, R., Gjelsvik, K.J., Losick, V.P., 2021. Wound-induced polyploidization is
927 dependent on Integrin-Yki signaling. Biology Open 10, bio055996.

928 Bi, D., Yang, X., Marchetti, M.C., Manning, M.L., 2016. Motility-driven glass and jamming
929 transitions in biological tissues. Phys Rev X 6.

930 Cao, J., Wang, J., Jackman, C.P., Cox, A.H., Trembley, M.A., Balowski, J.J., Cox, B.D., De
931 Simone, A., Dickson, A.L., Di Talia, S., Small, E.M., Kiehart, D.P., Bursac, N., Poss, K.D.,
932 2017. Tension Creates an Endoreplication Wavefront that Leads Regeneration of Epicardial
933 Tissue. Dev Cell 42, 600–615.e604.

934 Carriere, R., 1969. The growth of liver parenchymal nuclei and its endocrine regulation.
935 International review of cytology 25, 201–277.

936 Chernomordik, L.V., Kozlov, M.M., 2008. Mechanics of membrane fusion. Nature Structural &
937 Molecular Biology 15, 675–683.

938 Corbel, S.Y., Lee, A., Yi, L., Duenas, J., Brazelton, T.R., Blau, H.M., Rossi, F.M., 2003.
939 Contribution of hematopoietic stem cells to skeletal muscle. Nat Med 9, 1528–1532.

940 Davies, P.S., Powell, A.E., Swain, J.R., Wong, M.H., 2009. Inflammation and Proliferation Act
941 Together to Mediate Intestinal Cell Fusion. PloS one 4, e6530.

942 Dehn, A.S., Duhaime, L., Gogna, N., Nishina, P.M., Kelly, K., Losick, V.P., 2023. Epithelial
943 mechanics are maintained by inhibiting cell fusion with age in Drosophila. Journal of Cell
944 Science.

945 Farooqui, R., Fenteany, G., 2005. Multiple rows of cells behind an epithelial wound edge extend
946 cryptic lamellipodia to collectively drive cell-sheet movement. Journal of Cell Science 118,
947 51–63.

948 Galko, M.J., Krasnow, M.A., 2004. Cellular and Genetic Analysis of Wound Healing in
949 Drosophila Larvae. PLoS Biol 2, e239.

950 Gentric, G., Maillet, V., Paradis, V., Couton, D., L'Hermitte, A., Panasyuk, G., Fromenty, B.,
951 Celton-Morizur, S., Desdouets, C., 2015. Oxidative stress promotes pathologic
952 polyploidization in nonalcoholic fatty liver disease. J Clin Invest 125, 981–992.

953 Grendler, J., Lowgren, S., Mills, M., Losick, V.P., 2019. Wound-induced polyploidization is
954 driven by Myc and supports tissue repair in the presence of DNA damage. Development
955 146.

956 Guirao, B., Rigaud, S.U., Bosveld, F., Bailles, A., López-Gay, J., Ishihara, S., Sugimura, K.,
957 Graner, F., Bellaïche, Y., 2015. Unified quantitative characterization of epithelial tissue
958 development. eLife 4, e08519.

959 Han, I., Nassar, L.S., Page-McCaw, A., Hutson, M.S., 2023. After wounding, a G-protein
960 coupled receptor restores tension to epithelial cells in a dynamic inward-traveling wave.
961 bioRxiv.

962 Han, I.S., J., H., White, J.H., O'Connor, J.T., Nassar, L.S., Tro, K.J., Page-McCaw, A., Hutson,
963 M.S., 2024. After wounding, a G-protein coupled receptor promotes the restoration of
964 tension in epithelial cells. Molecular Biology of the Cell 35, ar66.

965 Horn, A., Raavicharla, S., Shah, S., Cox, D., Jaiswal, J.K., 2020. Mitochondrial fragmentation
966 enables localized signaling required for cell repair. J Cell Biol 219.

967 Illidge, T.M., Cragg, M.S., Fringes, B., Olive, P., Erenpreisa, J.A., 2000. Polyploid giant cells
968 provide a survival mechanism for p53 mutant cells after DNA damage. Cell Biol Int 24,
969 621–633.

970 Iosilevskii, Y., Podbilewicz, B., 2021. Chapter Seven - Programmed cell fusion in development
971 and homeostasis, in: Jarriault, S., Podbilewicz, B. (Eds.), Current Topics in Developmental
972 Biology. Academic Press, pp. 215–244.

973 Kakanj, P., Bhide, S., Moussian, B., Leptin, M., 2022. Autophagy-mediated plasma membrane
974 removal promotes the formation of epithelial syncytia. Embo j 41, e109992.

975 Kim, J.H., Jin, P., Duan, R., Chen, E.H., 2015a. Mechanisms of myoblast fusion during muscle
976 development. Current opinion in genetics & development 32, 162–170.

977 Kim, J.H., Ren, Y., Ng, W.P., Li, S., Son, S., Kee, Y.S., Zhang, S., Zhang, G., Fletcher, D.A.,
978 Robinson, D.N., Chen, E.H., 2015b. Mechanical tension drives cell membrane fusion. Dev
979 Cell 32, 561–573.

980 Lee, D.M., Chen, E.H., 2019. Drosophila Myoblast Fusion: Invasion and Resistance for the
981 Ultimate Union. Annu Rev Genet 53, 67–91.

982 Lehka, L., Rędowicz, M.J., 2020. Mechanisms regulating myoblast fusion: A multilevel
983 interplay. Seminars in Cell & Developmental Biology 104, 81–92.

984 Leroy, H., Han, M., Woottum, M., Bracq, L., Bouchet, J., Xie, M., Benichou, S., 2020. Virus-
985 Mediated Cell-Cell Fusion. Int J Mol Sci 21.

986 Losick, V.P., 2016. Wound-Induced Polyploidy Is Required for Tissue Repair. Adv Wound Care
987 (New Rochelle) 5, 271–278.

988 Losick, V.P., Duhaime, L.G., 2021. The endocycle restores tissue tension in the Drosophila
989 abdomen post wound repair. Cell Rep 37, 109827.

990 Losick, V.P., Fox, D.T., Spradling, A.C., 2013. Polyploidization and cell fusion contribute to
991 wound healing in the adult Drosophila epithelium. Curr Biol 23, 2224–2232.

992 Losick, V.P., Jun, A.S., Spradling, A.C., 2016. Wound-Induced Polyploidization: Regulation by
993 Hippo and JNK Signaling and Conservation in Mammals. PloS one 11, e0151251.

994 Madra, S., Styles, J., Smith, A.G., 1995. Perturbation of hepatocyte nuclear populations induced
995 by iron and polychlorinated biphenyls in C57BL/10ScSn mice during carcinogenesis.
996 Carcinogenesis 16, 719–727.

997 Markvoort, A.J., Marrink, S.J., 2011. Chapter 11 - Lipid Acrobatics in the Membrane Fusion
998 Arena, in: Chernomordik, L.V., Kozlov, M.M. (Eds.), Current Topics in Membranes.
999 Academic Press, pp. 259–294.

1000 Martin, P., Lewis, J., 1992. Actin cables and epidermal movement in embryonic wound healing.
1001 Nature 360, 179–183.

1002 Martin, P., Pardo-Pastor, C., Jenkins, R.G., Rosenblatt, J., 2024. Imperfect wound healing sets
1003 the stage for chronic diseases. Science 386, eadp2974.

1004 McNeil, P.L., Steinhardt, R.A., 2003. Plasma membrane disruption: repair, prevention,
1005 adaptation. Annu Rev Cell Dev Biol 19, 697–731.

1006 Mehaffey, T.M., Hecht, C.A., White, J.S., Hutson, M.S., Page-McCaw, A., 2024. Live imaging
1007 basement membrane assembly under the pupal notum epithelium. MicroPubl Biol 2024.

1008 Melzer, C., von der Ohe, J., Hass, R., 2018. In Vitro Fusion of Normal and Neoplastic Breast
1009 Epithelial Cells with Human Mesenchymal Stroma/Stem Cells Partially Involves Tumor
1010 Necrosis Factor Receptor Signaling. Stem Cells 36, 977–989.

1011 Meng, X., Yang, Q., Yu, X., Zhou, J., Ren, X., Zhou, Y., Xu, S., 2020. Actin Polymerization and
1012 ESCRT Trigger Recruitment of the Fusogens Syntaxin-2 and EFF-1 to Promote Membrane
1013 Repair in C. elegans. Dev Cell 54, 624–638 e625.

1014 Mohler, W.A., Shemer, G., del Campo, J.J., Valansi, C., Opoku-Serebuoh, E., Scranton, V.,
1015 Assaf, N., White, J.G., Podbilewicz, B., 2002. The type I membrane protein EFF-1 is
1016 essential for developmental cell fusion. Developmental cell 2, 355–362.

1017 Mohler, W.A., Simske, J.S., Williams-Masson, E.M., Hardin, J.D., White, J.G., 1998. Dynamics
1018 and ultrastructure of developmental cell fusions in the Caenorhabditis elegans hypodermis.
1019 Curr Biol 8, 1087–1090.

1020 Mosieniak, G., Sliwinska, M.A., Alster, O., Strzeszewska, A., Sunderland, P., Piechota, M., Was,
1021 H., Sikora, E., 2015. Polyploidy Formation in Doxorubicin-Treated Cancer Cells Can Favor
1022 Escape from Senescence. Neoplasia 17, 882–893.

1023 Muramatsu, Y., Yamada, T., Moralejo, D.H., Mochizuki, H., Sogawa, K., Matsumoto, K., 2000.
1024 Increased polyploid incidence is associated with abnormal copper accumulation in the liver
1025 of LEC mutant rat. Research Communications in Molecular Pathology and Pharmacology
1026 107, 129–136.

1027 Nandakumar, S., Grushko, O., Buttitta, L.A., 2020. Polyploidy in the adult Drosophila brain.
1028 Elife 9.

1029 Noma, K., Goncharov, A., Ellisman, M.H., Jin, Y., 2017. Microtubule-dependent ribosome
1030 localization in C. elegans neurons. eLife 6, e26376.

1031 Noubissi, F.K., Harkness, T., Alexander, C.M., Ogle, B.M., 2015. Apoptosis-induced cancer cell
1032 fusion: a mechanism of breast cancer metastasis. The FASEB Journal 29, 4036–4045.

1033 Nygren, J.M., Jovinge, S., Breitbach, M., Säwén, P., Röll, W., Hescheler, J., Taneera, J.,
1034 Fleischmann, B.K., Jacobsen, S.E., 2004. Bone marrow-derived hematopoietic cells
1035 generate cardiomyocytes at a low frequency through cell fusion, but not transdifferentiation.
1036 Nat Med 10, 494–501.

1037 O'Connor, J., Akbar, F.B., Hutson, M.S., Page-McCaw, A., 2021a. Zones of cellular damage
1038 around pulsed-laser wounds. PLoS One 16, e0253032.

1039 O'Connor, J.T., Shannon, E.K., Hutson, M.S., Page-McCaw, A., 2022. Mounting Drosophila
1040 pupae for laser ablation and live imaging of the dorsal thorax. STAR Protocols 3, 101396.

1041 O'Connor, J.T., Stevens, A.C., Shannon, E.K., Akbar, F.B., LaFever, K.S., Narayanan, N.P.,
1042 Gailey, C.D., Hutson, M.S., Page-McCaw, A., 2021b. Proteolytic activation of Growth-
1043 blocking peptides triggers calcium responses through the GPCR Mthl10 during epithelial
1044 wound detection. Developmental Cell 56, 2160–2175.e2165.

1045 Ogden, A., Rida, P.C.G., Knudsen, B.S., Kucuk, O., Aneja, R., 2015. Docetaxel-induced
1046 polyploidization may underlie chemoresistance and disease relapse. Cancer Letters 367, 89–
1047 92.

1048 Ogura, Y., Wen, F.-L., Sami, M.M., Shibata, T., Hayashi, S., 2018. A Switch-like Activation
1049 Relay of EGFR-ERK Signaling Regulates a Wave of Cellular Contractility for Epithelial
1050 Invagination. Developmental Cell 46, 162–172.e165.

1051 Park, J.A., Kim, J.H., Bi, D., Mitchel, J.A., Qazvini, N.T., Tantisira, K., Park, C.Y., McGill, M.,
1052 Kim, S.H., Gweon, B., Notbohm, J., Steward, R., Jr., Burger, S., Randell, S.H., Kho, A.T.,
1053 Tambe, D.T., Hardin, C., Shore, S.A., Israel, E., Weitz, D.A., Tschumperlin, D.J., Henske,
1054 E.P., Weiss, S.T., Manning, M.L., Butler, J.P., Drazen, J.M., Fredberg, J.J., 2015.
1055 Unjamming and cell shape in the asthmatic airway epithelium. Nat Mater 14, 1040–1048.

1056 Pawelek, J.M., Chakraborty, A.K., 2008. Fusion of tumour cells with bone marrow-derived cells:
1057 a unifying explanation for metastasis. Nature Reviews Cancer 8, 377–386.

1058 Petrany, M.J., Millay, D.P., 2019. Cell Fusion: Merging Membranes and Making Muscle. Trends
1059 Cell Biol 29, 964–973.

1060 Pignoni, F., Zipursky, S.L., 1997. Induction of Drosophila eye development by Decapentaplegic.
1061 Development 124, 271–278.

1062 Podbilewicz, B., Leikina, E., Sapir, A., Valansi, C., Suissa, M., Shemer, G., Chernomordik, L.V.,
1063 2006. The C. elegans developmental fusogen EFF-1 mediates homotypic fusion in
1064 heterologous cells and in vivo. Developmental cell 11, 471–481.

1065 Podbilewicz, B., White, J.G., 1994. Cell fusions in the developing epithelial of C. elegans. Dev
1066 Biol 161, 408–424.

1067 Powell, A.E., Anderson, E.C., Davies, P.S., Silk, A.D., Pelz, C., Impey, S., Wong, M.H., 2011.
1068 Fusion between Intestinal epithelial cells and macrophages in a cancer context results in
1069 nuclear reprogramming. Cancer Res 71, 1497–1505.

1070 Qu, Y., Zhang, L., Rong, Z., He, T., Zhang, S., 2013. Number of glioma polyploid giant cancer
1071 cells (PGCCs) associated with vasculogenic mimicry formation and tumor grade in human
1072 glioma. J Exp Clin Cancer Res 32, 75.

1073 Renaud, S.J., Jeyarajah, M.J., 2022. How trophoblasts fuse: an in-depth look into placental
1074 syncytiotrophoblast formation. Cellular and Molecular Life Sciences 79, 433.

1075 Rushton, E., Drysdale, R., Abmayr, S.M., Michelson, A.M., Bate, M., 1995. Mutations in a novel
1076 gene, myoblast city, provide evidence in support of the founder cell hypothesis for
1077 Drosophila muscle development. Development 121, 1979–1988.

1078 Sapir, A., Choi, J., Leikina, E., Avinoam, O., Valansi, C., Chernomordik, L.V., Newman, A.P.,
1079 Podbilewicz, B., 2007. AFF-1, a FOS-1-regulated fusogen, mediates fusion of the anchor
1080 cell in C. elegans. Developmental cell 12, 683–698.

1081 Scepanovic, G., Hunter, M.V., Kafri, R., Fernandez-Gonzalez, R., 2021. p38-mediated cell
1082 growth and survival drive rapid embryonic wound repair. Cell Reports 37, 109874.

1083 Sens, K.L., Zhang, S., Jin, P., Duan, R., Zhang, G., Luo, F., Parachini, L., Chen, E.H., 2010. An
1084 invasive podosome-like structure promotes fusion pore formation during myoblast fusion. J
1085 Cell Biol 191, 1013–1027.

1086 Shannon, E.K., Stevens, A., Edrington, W., Zhao, Y., Jayasinghe, A.K., Page-McCaw, A.,
1087 Hutson, M.S., 2017. Multiple Mechanisms Drive Calcium Signal Dynamics around Laser-
1088 Induced Epithelial Wounds. Biophysical Journal 113, 1623–1635.

1089 Shemer, G., Suissa, M., Kolotuev, I., Nguyen, K.C., Hall, D.H., Podbilewicz, B., 2004. EFF-1 is
1090 sufficient to initiate and execute tissue-specific cell fusion in C. elegans. Current Biology
1091 14, 1587–1591.

1092 Sigal, S.H., Rajvanshi, P., Gorla, G.R., Sokhi, R.P., Saxena, R., Gebhard Jr, D.R., Reid, L.M.,
1093 Gupta, S., 1999. Partial hepatectomy-induced polyploidy attenuates hepatocyte replication
1094 and activates cell aging events. American Journal of Physiology-Gastrointestinal and Liver
1095 Physiology 276, G1260–G1272.

1096 Søe, K., 2020. Osteoclast Fusion: Physiological Regulation of Multinucleation through
1097 Heterogeneity-Potential Implications for Drug Sensitivity. Int J Mol Sci 21.

1098 Song, Y., Zhao, Y., Deng, Z., Zhao, R., Huang, Q., 2021. Stress-Induced Polyploid Giant Cancer
1099 Cells: Unique Way of Formation and Non-Negligible Characteristics. Front Oncol 11,
1100 724781.

1101 Stringer, C., Wang, T., Michaelos, M., Pachitariu, M., 2021. Cellpose: a generalist algorithm for
1102 cellular segmentation. Nat Methods 18, 100–106.

1103 Tamada, M., Perez, T.D., Nelson, W.J., Sheetz, M.P., 2007. Two distinct modes of myosin
1104 assembly and dynamics during epithelial wound closure. J. Cell Biol. 176, 27–33.

1105 Tamori, Y., Deng, W.M., 2013. Tissue repair through cell competition and compensatory cellular
1106 hypertrophy in postmitotic epithelia. Dev Cell 25, 350–363.

1107 Tetley, R.J., Staddon, M.F., Heller, D., Hoppe, A., Banerjee, S., Mao, Y., 2019. Tissue Fluidity
1108 Promotes Epithelial Wound Healing. Nat Phys 15, 1195–1203.

1109 Toyoda, H., Bregerie, O., Vallet, A., Nalpas, B., Pivert, G., Brechot, C., Desdouets, C., 2005.
1110 Changes to hepatocyte ploidy and binuclearity profiles during human chronic viral hepatitis.
1111 Gut 54, 297–302.

1112 Wang, X., Merkel, M., Sutter, L.B., Erdemci-Tandogan, G., Manning, M.L., Kasza, K.E., 2020.
1113 Anisotropy links cell shapes to tissue flow during convergent extension. Proc Natl Acad Sci
1114 U S A 117, 13541–13551.

1115 Wang, Y., Antunes, M., Anderson, A.E., Kadrmas, J.L., Jacinto, A., Galko, M.J., 2015. Integrin
1116 Adhesions Suppress Syncytium Formation in the Drosophila Larval Epidermis. Current
1117 Biology 25, 2215–2227.

1118 Wang, Y., Wang, Y., Zheng, W., 2013. Cytologic changes of ovarian epithelial cancer induced
1119 by neoadjuvant chemotherapy. Int J Clin Exp Pathol 6, 2121–2128.

1120 Weihua, Z., Lin, Q., Ramoth, A.J., Fan, D., Fidler, I.J., 2011. Formation of solid tumors by a
1121 single multinucleated cancer cell. Cancer 117, 4092–4099.

1122 Wheatley, D., 2008. Growing evidence of the repopulation of regressed tumours by the division
1123 of giant cells. Cell Biology International 32, 1029–1030.

1124 White, J., Hutson, M.S., Page-McCaw, A., 2024. Wounding increases nuclear ploidy in wound-
1125 proximal epidermal cells of the Drosophila pupal notum. MicroPubl Biol 2024.

1126 Wilkinson, P.D., Alencastro, F., Delgado, E.R., Leek, M.P., Weirich, M.P., Otero, P.A., Roy, N.,
1127 Brown, W.K., Oertel, M., Duncan, A.W., 2019. Polyploid Hepatocytes Facilitate Adaptation
1128 and Regeneration to Chronic Liver Injury. Am J Pathol 189, 1241–1255.

1129 Zhang, H., Ma, H., Yang, X., Fan, L., Tian, S., Niu, R., Yan, M., Zheng, M., Zhang, S., 2021.
1130 Cell Fusion-Related Proteins and Signaling Pathways, and Their Roles in the Development
1131 and Progression of Cancer. Front Cell Dev Biol 9, 809668.

1132 Zhao, Q., Zhang, K., Li, Z., Zhang, H., Fu, F., Fu, J., Zheng, M., Zhang, S., 2021. High
1133 Migration and Invasion Ability of PGCCs and Their Daughter Cells Associated With the
1134 Nuclear Localization of S100A10 Modified by SUMOylation. Front Cell Dev Biol 9,
1135 696871.

1136

Figure 1

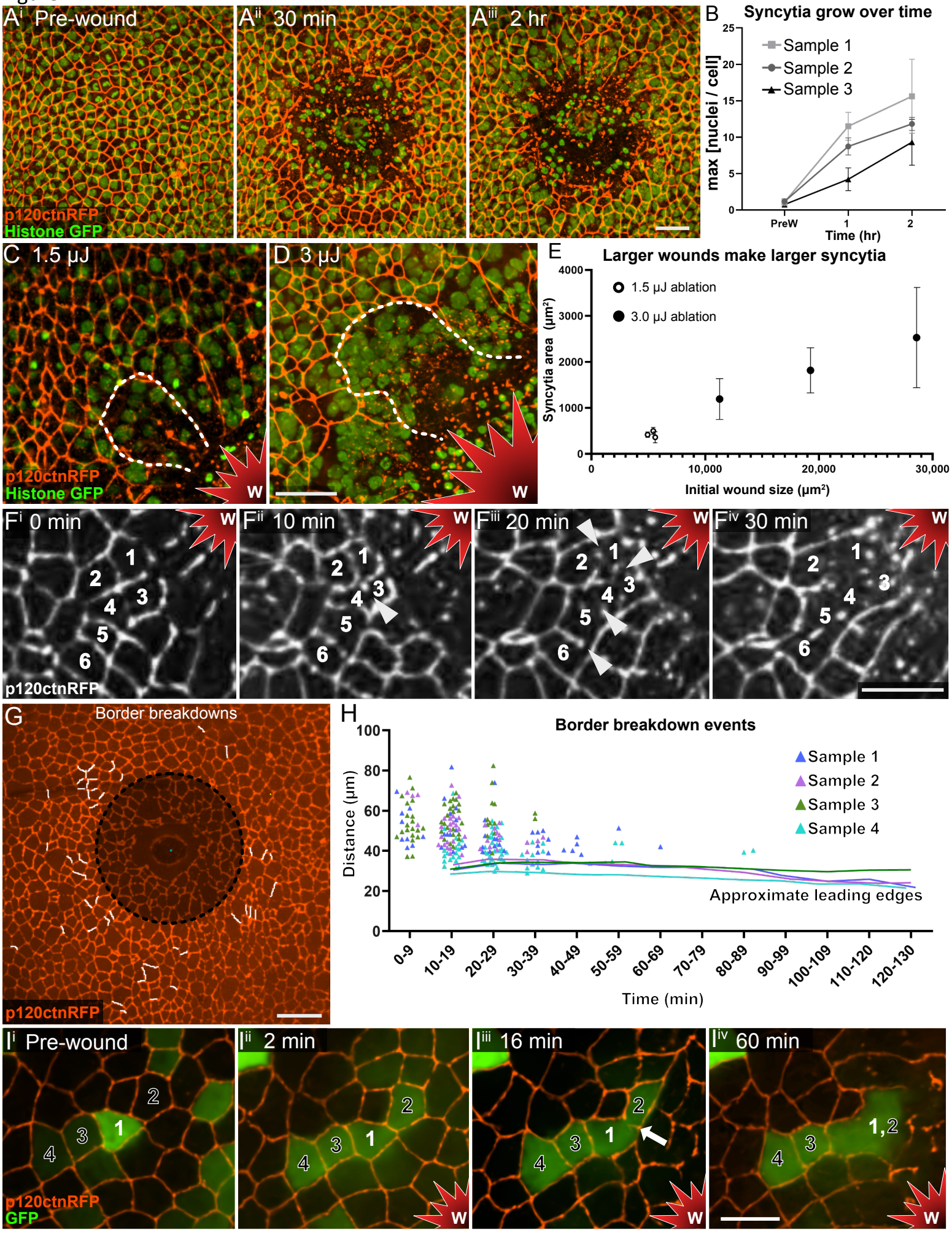
Aⁱ Pre-wound
Aⁱⁱ 30 min
Aⁱⁱⁱ 2 hr
p120ctnRFP
Histone GFP
B
Syncytia grow over time
Sample 1
Sample 2
Sample 3
max [nuclei / cell]
PreW
1
2
Time (hr)
C 1.5 µJ
D 3 µJ
p120ctnRFP
Histone GFP
W
E
Larger wounds make larger syncytia
1.5 µJ ablation
3.0 µJ ablation
Syncytia area (µm²)
Initial wound size (µm²)
Fⁱ 0 min
Fⁱⁱ 10 min
Fⁱⁱⁱ 20 min
Fⁱᵛ 30 min
p120ctnRFP
G
Border breakdowns
p120ctnRFP
H
Border breakdown events
Sample 1
Sample 2
Sample 3
Sample 4
Distance (µm)
Approximate leading edges
Time (min)
Iⁱ Pre-wound
Iⁱⁱ 2 min
Iⁱⁱⁱ 16 min
Iⁱᵛ 60 min
p120ctnRFP
GFP

Figure 2

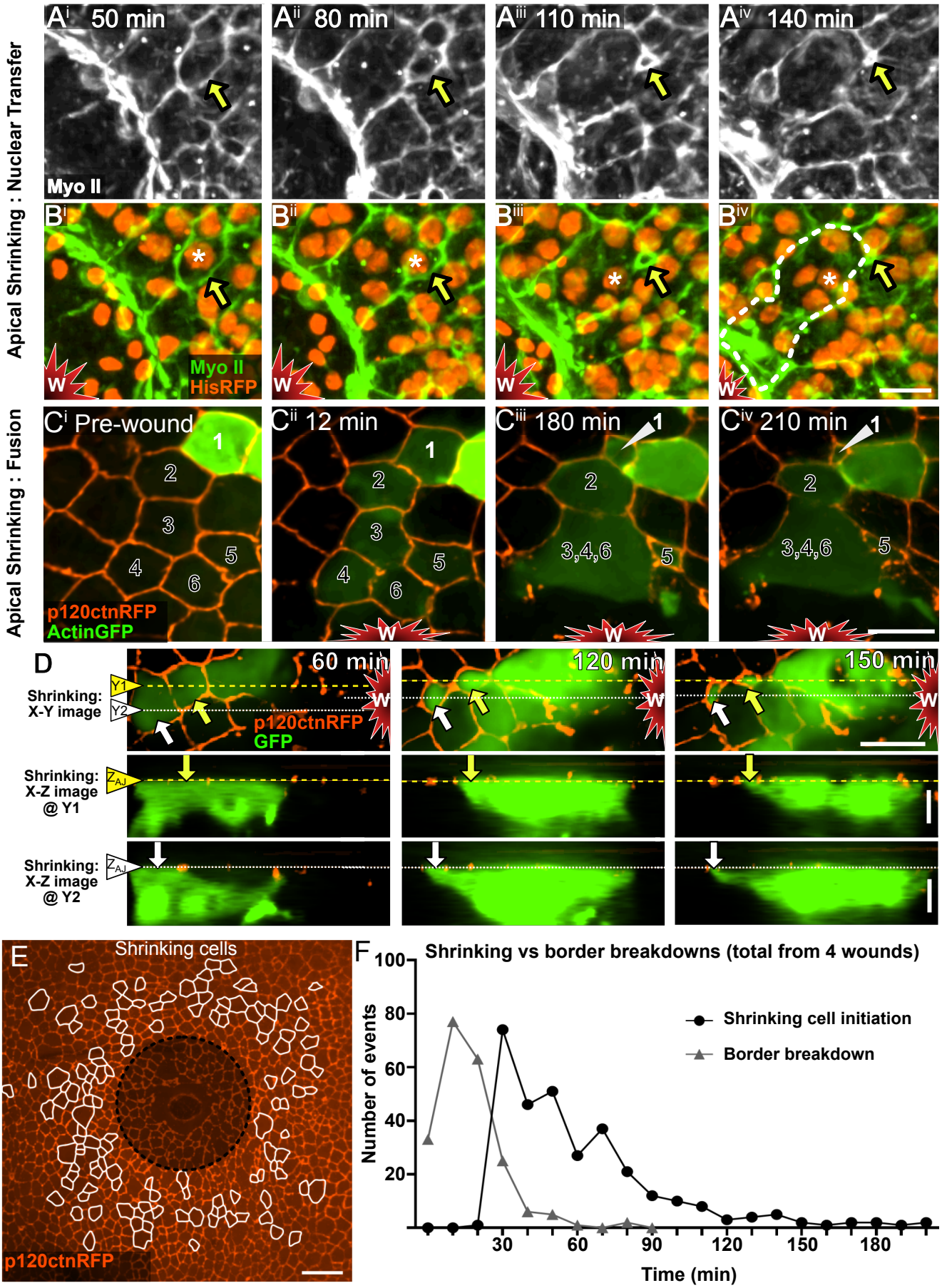
Apical Shrinking : Nuclear Transfer
Ai 50 min
Aii 80 min
Aiii 110 min
Aiv 140 min
Myo II
Bi
Bii
Biii
Biv
Myo II
HisRFP
W
Apical Shrinking : Fusion
Ci Pre-wound
Cii 12 min
Ciii 180 min
Civ 210 min
1
2
3
4
5
6
3,4,6
p120ctnRFP
ActinGFP
D
60 min
120 min
150 min
Shrinking: X-Y image
Y1
Y2
p120ctnRFP
GFP
Shrinking: X-Z image @ Y1
Shrinking: X-Z image @ Y2
ZAJ
E
Shrinking cells
p120ctnRFP
F
Shrinking vs border breakdowns (total from 4 wounds)
Number of events
Time (min)
Shrinking cell initiation
Border breakdown
100
80
60
40
20
30
60
90
120
150
180

Figure 3

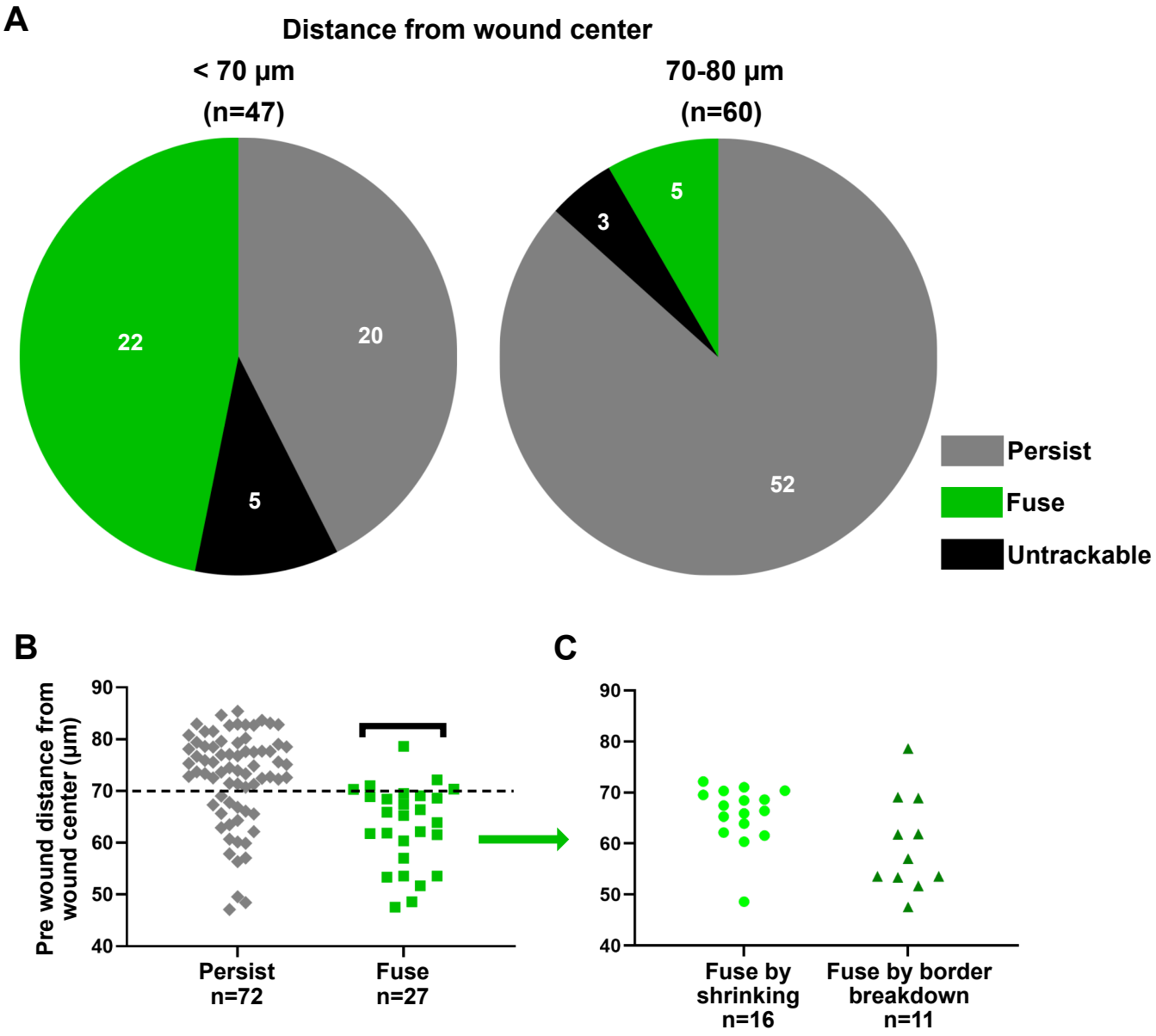
A
Distance from wound center
< 70 µm
(n=47)
70-80 µm
(n=60)
20
22
5
5
3
52
Persist
Fuse
Untrackable
B
C
Pre wound distance from wound center (µm)
90
80
70
60
50
40
Persist
n=72
Fuse
n=27
Fuse by shrinking
n=16
Fuse by border breakdown
n=11

Figure 4

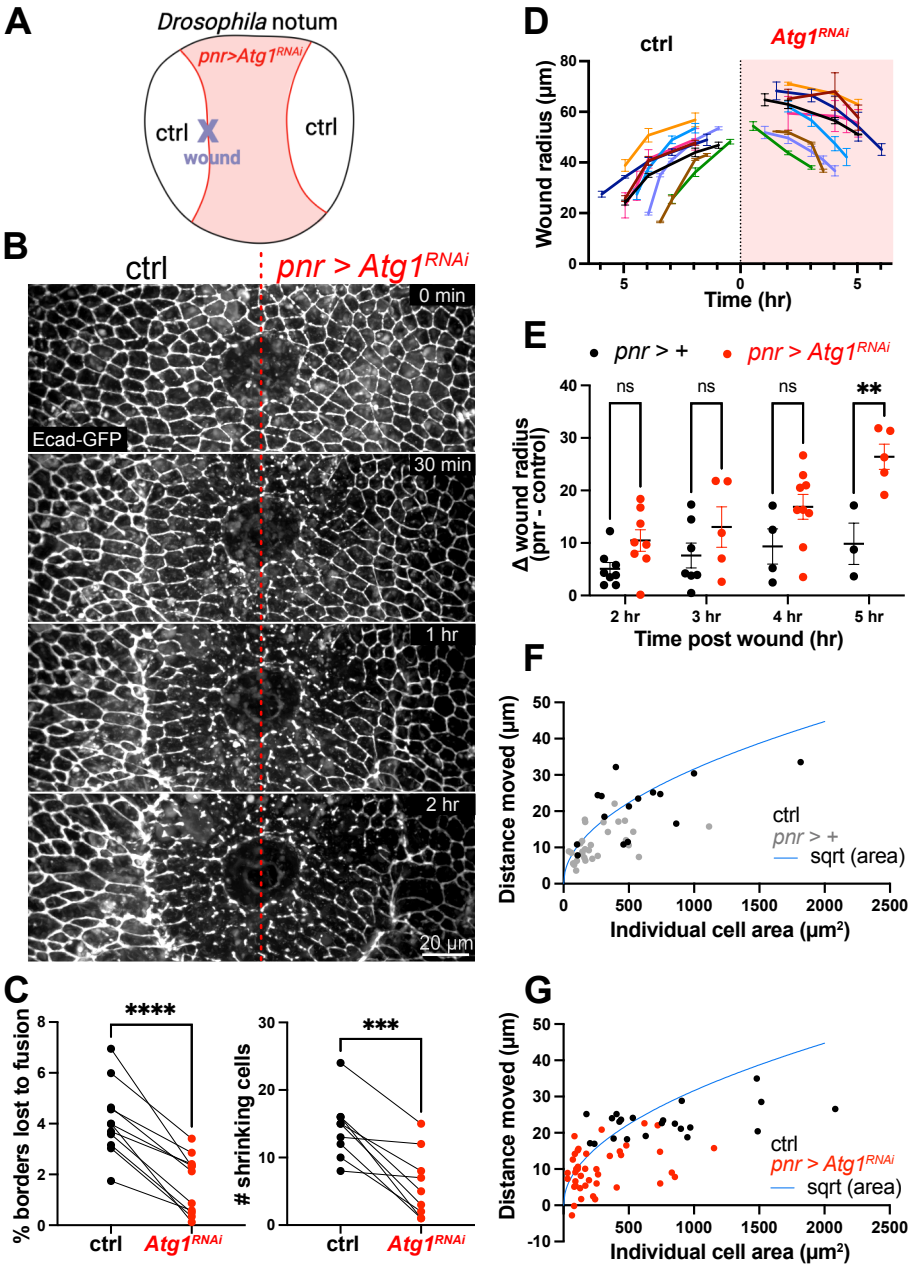
A
Drosophila notum
pnr>Atg1RNAi
ctrl
wound
ctrl
B
ctrl
pnr > Atg1RNAi
0 min
Ecad-GFP
30 min
1 hr
2 hr
20 µm
C
% borders lost to fusion
****
ctrl
Atg1RNAi
shrinking cells
***
ctrl
Atg1RNAi
D
ctrl
Atg1RNAi
Wound radius (µm)
Time (hr)
E
pnr > +
pnr > Atg1RNAi
Δ wound radius (pnr - control)
ns
ns
ns
**
2 hr
3 hr
4 hr
5 hr
Time post wound (hr)
F
Distance moved (µm)
ctrl
pnr > +
sqrt (area)
Individual cell area (µm²)
G
Distance moved (µm)
ctrl
pnr > Atg1RNAi
sqrt (area)
Individual cell area (µm²)

Figure 5

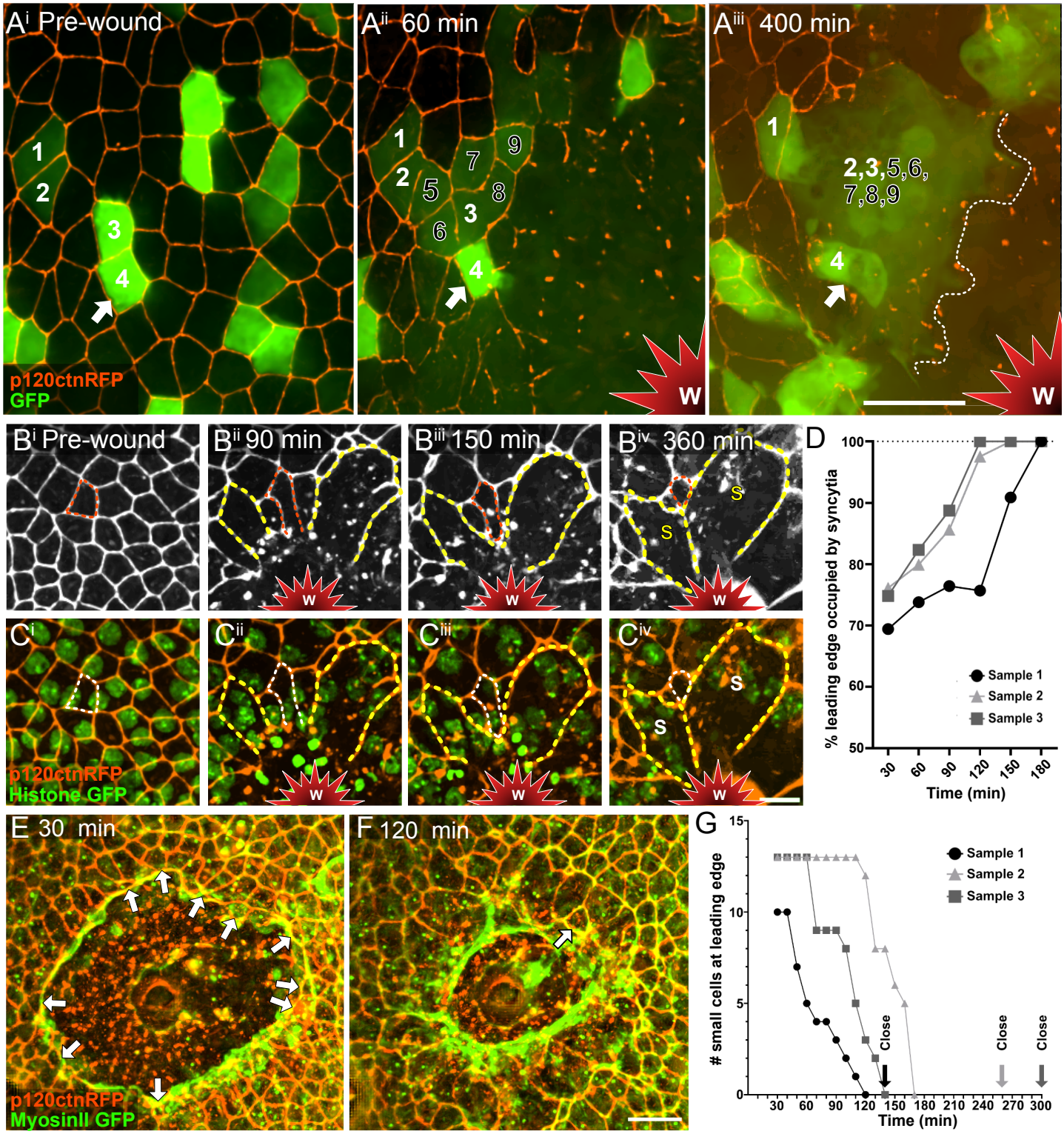
A^i Pre-wound
A^ii 60 min
A^iii 400 min
1
2
3
4
5
6
7
8
9
2,3,5,6,
7,8,9
p120ctnRFP
GFP
W
B^i Pre-wound
B^ii 90 min
B^iii 150 min
B^iv 360 min
S
C^i
C^ii
C^iii
C^iv
p120ctnRFP
Histone GFP
D
% leading edge occupied by syncytia
Time (min)
Sample 1
Sample 2
Sample 3
E 30 min
F 120 min
p120ctnRFP
MyosinII GFP
G
small cells at leading edge
Close

Figure 6

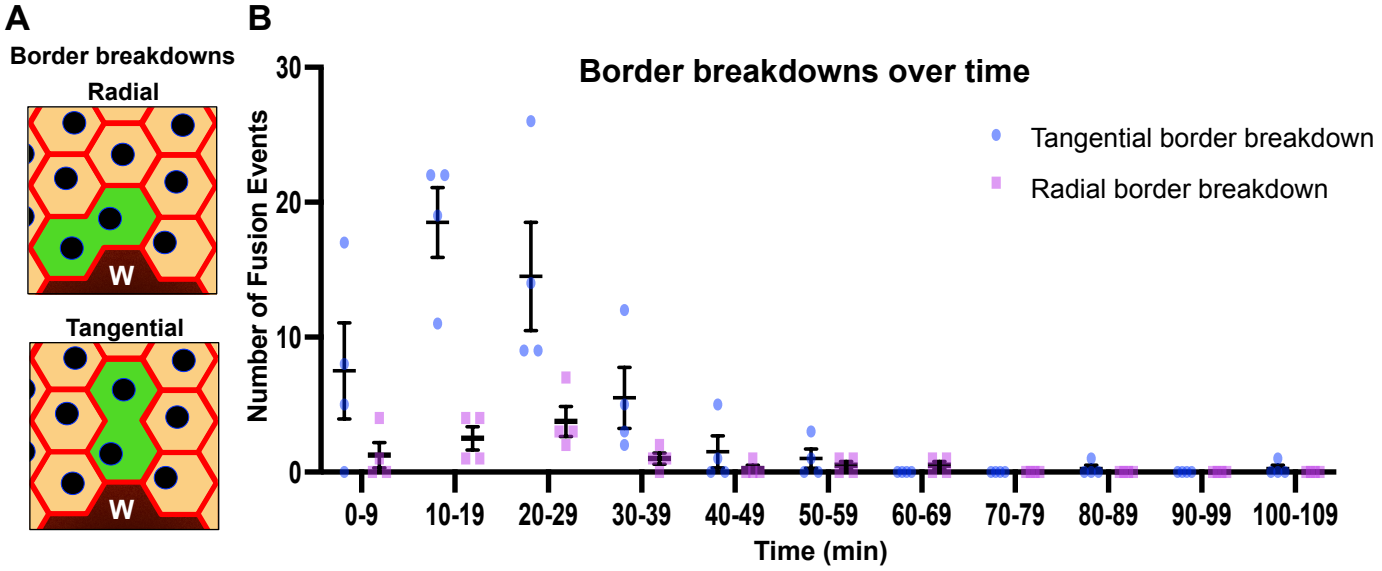

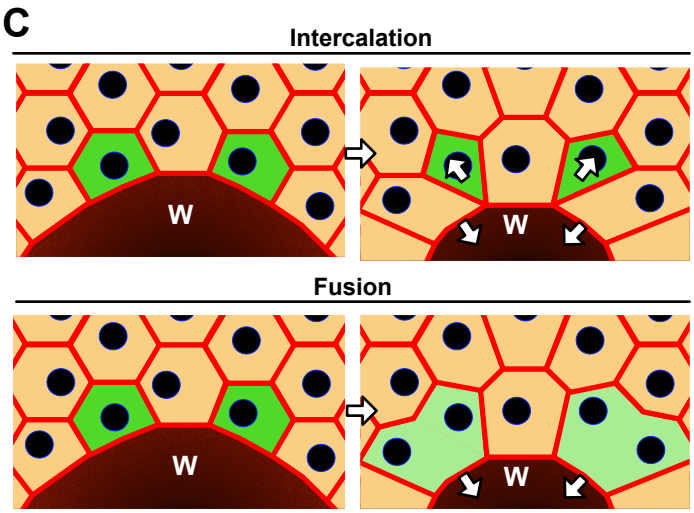

D

	Sample number 1	2	3
Time of closure (min)	140	260	300
# cells lost from leading edge	39	43	42
by fusion	16 (41%)	15 (35%)	7 (17%)
by intercalation	23 (59%)	28 (65%)	35 (83%)

Figure 7

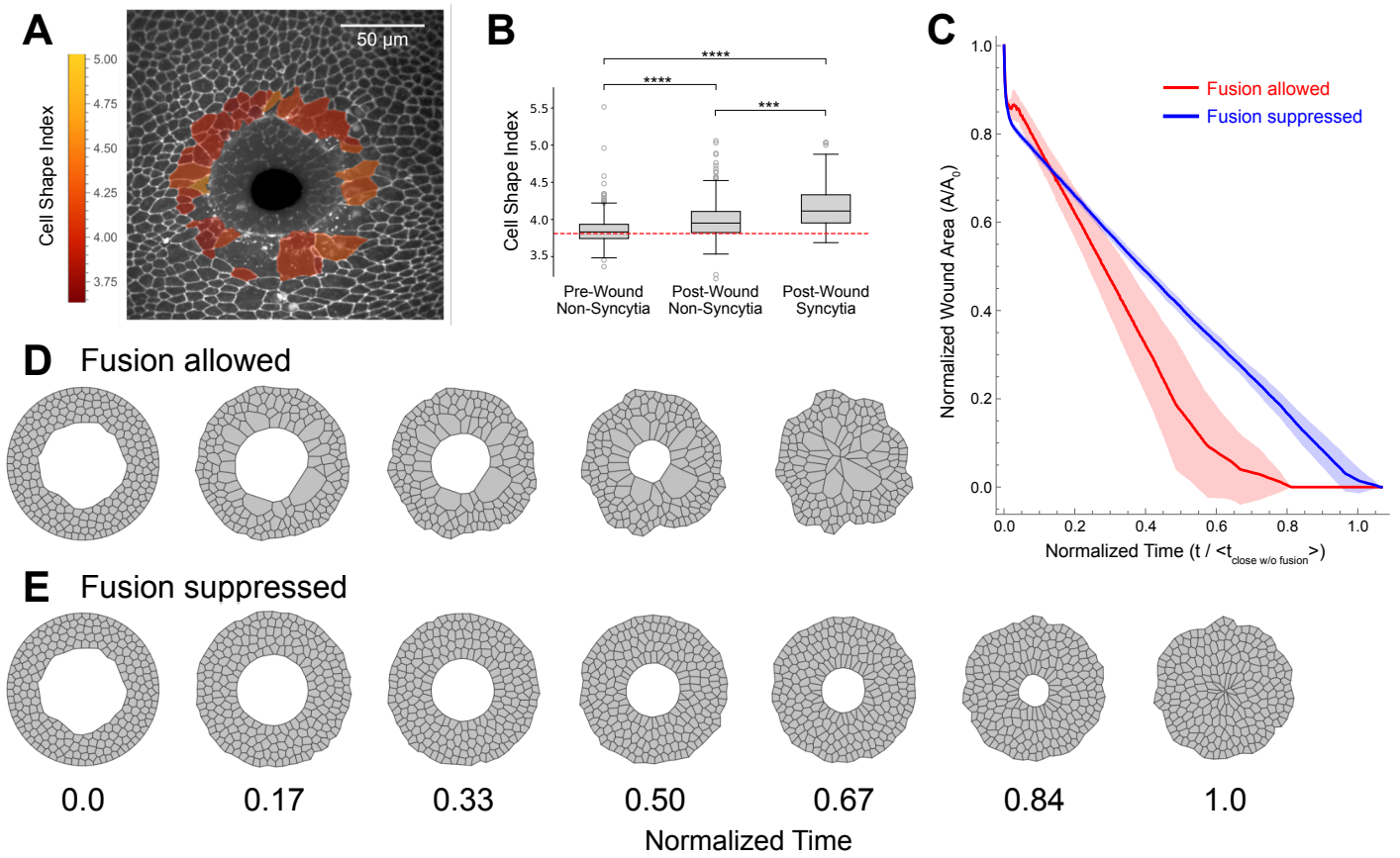
A
50 µm
Cell Shape Index
5.00
4.75
4.50
4.25
4.00
3.75
B
Cell Shape Index
5.5
5.0
4.5
4.0
3.5
****
****
***
Pre-Wound Non-Syncytia
Post-Wound Non-Syncytia
Post-Wound Syncytia
C
Normalized Wound Area (A/A0)
1.0
0.8
0.6
0.4
0.2
0.0
Fusion allowed
Fusion suppressed
0.0
0.2
0.4
0.6
0.8
1.0
Normalized Time (t / <tclose w/o fusion>)
D Fusion allowed
E Fusion suppressed
0.0
0.17
0.33
0.50
0.67
0.84
1.0
Normalized Time

Figure 8

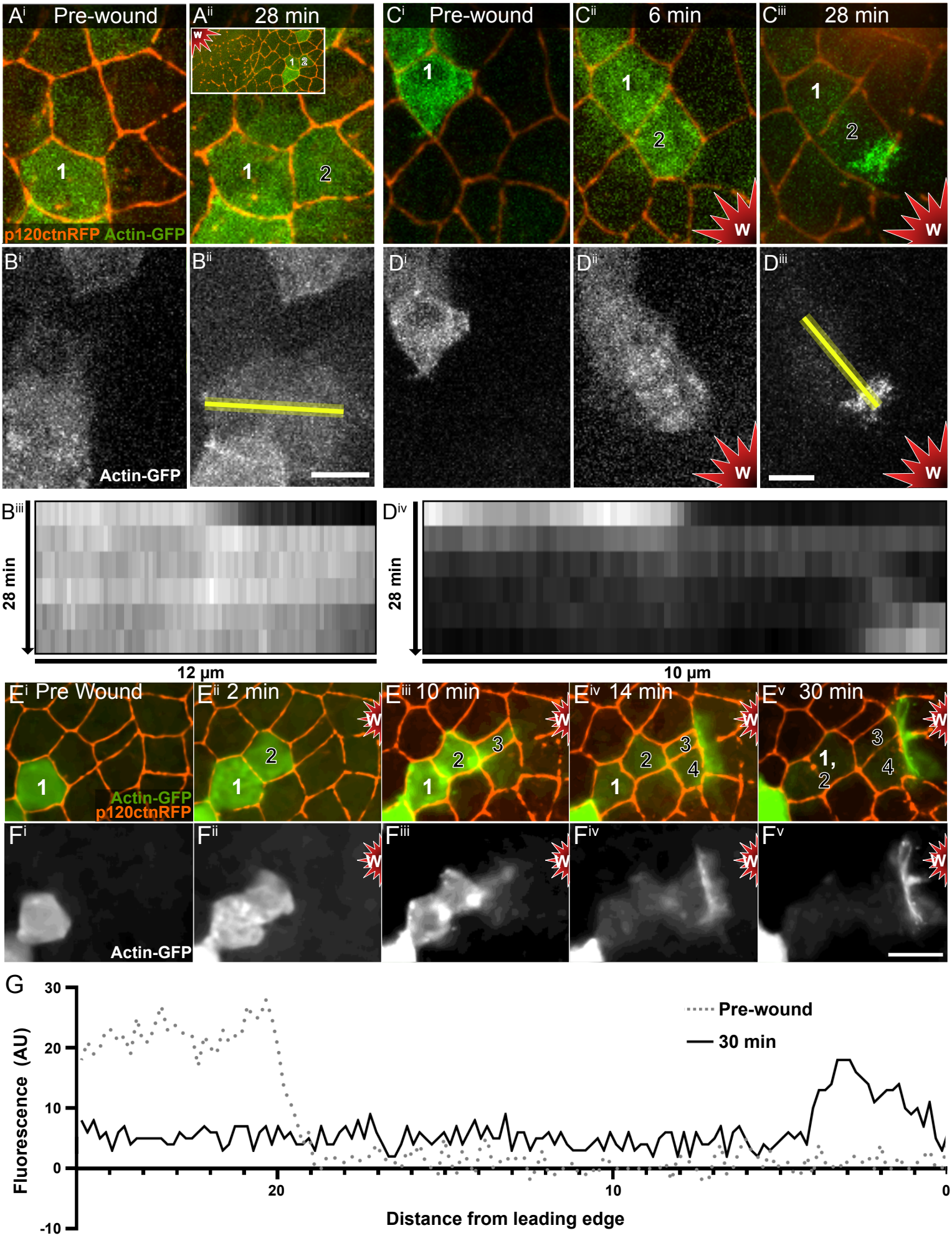
A^i Pre-wound
A^ii 28 min
C^i Pre-wound
C^ii 6 min
C^iii 28 min
p120ctnRFP Actin-GFP
Actin-GFP
B^iii
D^iv
28 min
12 µm
10 µm
E^i Pre Wound
E^ii 2 min
E^iii 10 min
E^iv 14 min
E^v 30 min
Actin-GFP
p120ctnRFP
F^i
F^ii
F^iii
F^iv
F^v
G
Fluorescence (AU)
Distance from leading edge
Pre-wound
30 min

Figure 1—figure supplement 1

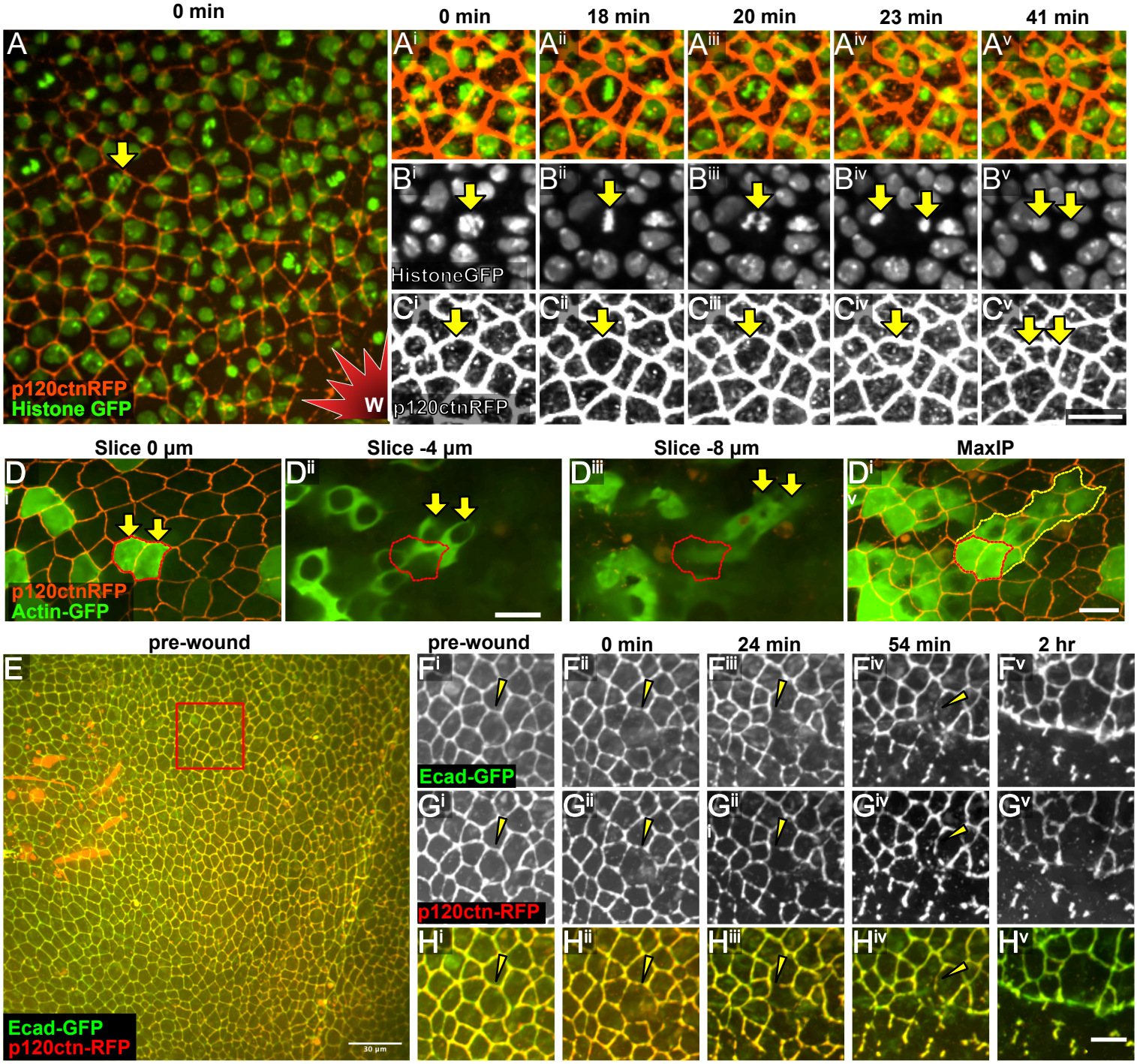

Figure 3 —figure supplement 1

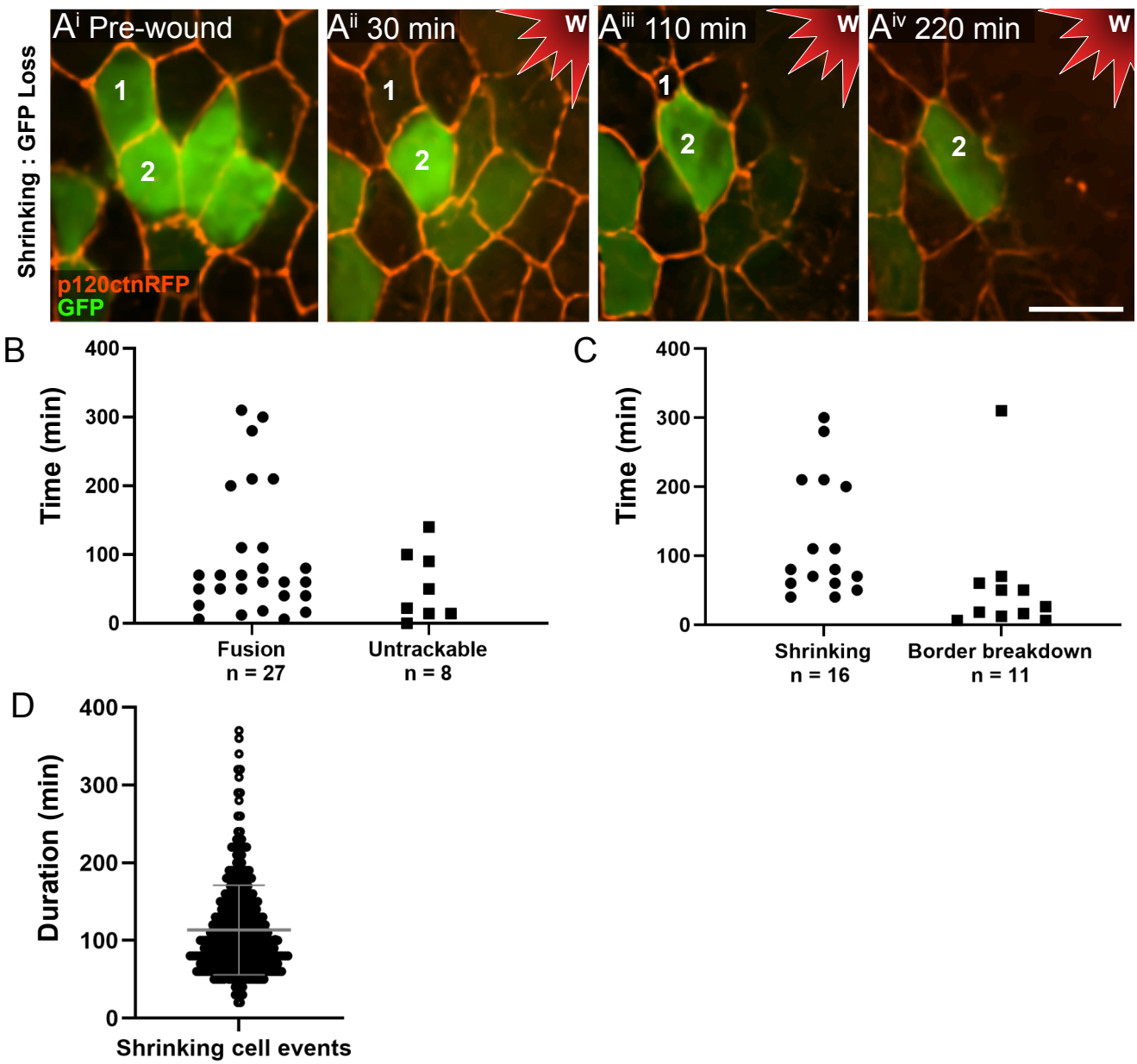

Figure 6 —figure supplement 1

A

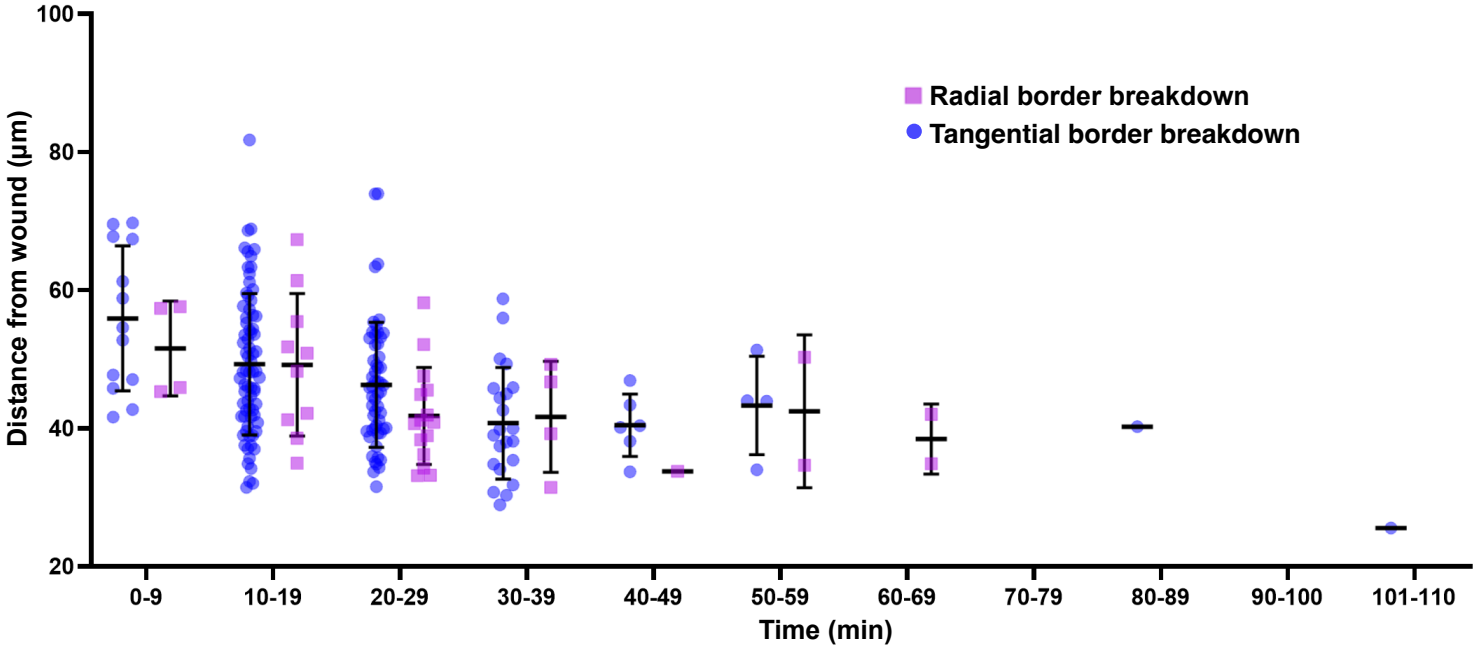
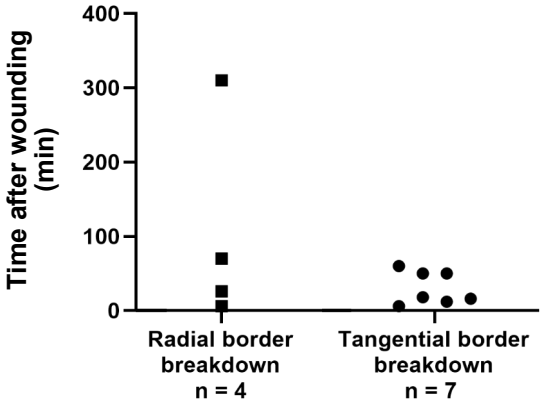
B